GTPase activating protein DLC1 spatio-temporally regulates Rho signaling

Lucien Hinderling[1,2,†], Max Heydasch[1,†], Giliane Rochat[1], Laurent Dubied[1], Jakobus van Unen[1], Maciej Dobrzynski[1], Olivier Pertz[1,*]

[1]Institute of Cell Biology, University of Bern, 3012 Bern, Switzerland

[2]Graduate School for Cellular and Biomedical Sciences, University of Bern, Switzerland

[†] These authors contributed equally to this work

[*] Corresponding author: olivier.pertz@unibe.ch

Abstract

Tightly regulated spatio-temporal Rho GTPase activity patterns regulate morphogenetic processes such as cell migration. Emerging evidence suggests that binding of Guanine nucleotide exchange factors (GEFs) and GTPase activating proteins (GAPs) to the cytoskeleton or adhesions mediate feedback regulation to spatio-temporal Rho GTPase activation. To explore such feedback regulation, we study the Rho specific GAP Deleted in Liver Cancer 1 (DLC1) which binds to focal adhesions (FAs) through mechanosensitive interactions. Using a FRET biosensor, we show that DLC1 loss of function leads to global increase in Rho activity and contractility throughout the cell without affecting a striking lamellar RhoA activity band in fibroblasts. Although RhoA activity may appear steady at the population level, individual molecules are continually activated by GEFs, inactivated by GAPs, and diffusing between subcellular regions, a dynamic turnover referred to as “signaling flux”. To directly measure this flux, we built a genetic circuit combining an optogenetic actuator to control Rho activity with a Rho activity biosensor. In spreading cells at steady state, optogenetic manipulation of Rho activity reveals that DLC1 controls the rate of Rho activation rather than duration, both at FAs and at the plasma membrane (PM). Local and reversible optogenetic control of contractility shows that DLC1 associates/dissociates with FAs during their reinforcement/relaxation. This might provide positive feedback that locally increases the rate of Rho activation at FAs that experience local tension to facilitate FA disassembly. Our results indicate that DLC1 operates both at the PM and at FAs to regulate global Rho activity levels at steady state, or to amplify local Rho activity at FAs experiencing a strong mechanical input, presumably to induce robust FA disassembly. This provides new insights in the complexity of spatio-temporal Rho GTPase signaling.

Introduction

Rho GTPases regulate the cytoskeletal dynamics that power morphogenetic processes at the cell- and tissue level (Etienne-Manneville and Hall, 2002). Their activity is tightly controlled in time and space by GEFs and GAPs, which respectively activate and inhibit Rho GTPases. In the GTP-loaded, active state, Rho GTPases bind downstream effectors that regulate cytoskeletal dynamics and other cellular processes. Based on classic experiments that include measuring population-averaged Rho GTPase activity levels, as well as overexpressing dominant positive/negative Rho GTPase mutants, it was proposed that Rac1 controls lamellipodial protrusion, Cdc42 regulates filopodium formation, and RhoA controls myosin-based contractility.

Recent studies in which spatio-temporal Rho GTPase activation dynamics were measured using fluorescence resonance energy transfer (FRET)-based biosensors, revealed a much higher signaling complexity. During cell migration, RhoA, Rac1 and Cdc42 are all activated in membrane protrusions at the leading edge (Itoh et al., 2002; Kraynov et al., 2000; Nalbant et al., 2004; Pertz et al., 2006). Further, the three Rho GTPases are activated in specific spatio-temporal sequences during the protrusion/retraction cycles that fluctuate on time and length scales of seconds and single micrometers (Machacek et al., 2009). A further level of complexity is that these Rho GTPase activity sequences vary depending on the cell system (Hu et al., 2022; Machacek et al., 2009; Martin et al., 2016). This indicates that complex spatio-temporal Rho GTPase signaling programs regulate processes such as cell migration. Similarly as for Ras GTPases (Schmick et al., 2015), it is now clear that these Rho GTPase signaling patterns most likely result from a precise spatio-temporal regulation of Rho GTPase signaling fluxes controlled by GEFs and GAPs (Bement and von Dassow, 2014; Fritz and Pertz, 2016a; Miller and Bement, 2009; Pertz, 2010). In this signaling flux, specific GEFs will be locally activated to load Rho GTPases with GTP depending on different cellular inputs. These GTP-loaded GTPases will then subsequently diffuse in the plasma membrane (PM) by virtue of their C-terminal lipid moiety until they encounter a locally activated GAP which eventually deactivates them. The interplay of GEFs, GAPs and diffusion of Rho GTPases in the PM will ultimately lead to the formation of a Rho GTPase activity pattern. Modelling studies have suggested that sophisticated dynamic signaling behaviors can emerge from the interplay of GEFs, GAPs, and GTPases within a signaling network (Tsyganov et al., 2012). Steady-state images of Rho GTPase activity patterns do not provide information about the whole Rho GTPase flux mentioned above.

This signaling complexity is consistent with the large amount of GEFs and GAPs that are ubiquitously expressed in cells (Fusco et al., 2016, 2016; Moon and Zheng, 2003; Mosaddeghzadeh and Ahmadian, 2021; Müller et al., 2020; Rossman et al., 2005). Recently, a system-wide screen has revealed that many GEFs and GAPS localize to

74 cytoskeletal structures as well as adhesion complexes such as focal adhesions (FAs)
75 (Müller et al., 2020). This strongly suggests the existence of feedback mechanisms from
76 the cytoskeleton and FAs to Rho GTPase signaling. In this study, it was shown that Rac1-
77 specific GEFs bind to FAs at the front, while Rac1-specific GAPs bind to FAs and at the
78 back of the lamella of fibroblasts. This precise, asymmetric positioning of GEFs and GAPs
79 might then regulate the Rho GTPase flux that produces the wide gradient of Rac activity
80 observed at the leading edge of fibroblasts (Itoh et al., 2002; Kraynov et al., 2000; Martin
81 et al., 2016). Such feedback regulation might allow leading edge Rac1 activity to constantly
82 integrate mechanosensitive inputs from FAs, allowing dynamic regulation of Rac1 activity
83 required to fine tune cell migration. Another prominent example of such spatio-temporal
84 feedback regulation are the excitable RhoA activity patterns observed in the cortex during
85 cytokinesis in *Xenopus Laevis* (Bement and von Dassow, 2014), that have also been
86 observed in mammalian cells (Graessl et al., 2017). Here, RhoA activity waves that control
87 F-actin wave patterns are spatially regulated by a RhoGAP that is locally regulated by F-
88 actin (Bement et al., 2015). Thus, cytoskeletal feedback to Rho GTPase regulation might
89 be crucial to generate dynamic Rho GTPase signaling patterns. Understanding such
90 spatio-temporal feedback regulation is not accessible with classic genetic approaches in
91 which long term perturbation of Rho GTPases, their regulators and effectors rapidly result
92 in a new mechanochemical state of the cell, that will not be informative about an initial
93 signaling/mechanical state of interest (Isogai and Danuser, 2018). Further, it is currently
94 unknown which specific features of spatio-temporal Rho GTPase signaling are regulated
95 to produce signaling patterns. For example, does negative regulation by a GAP solely
96 control Rho GTPase signal termination, or could it also modulate, less intuitive parameters
97 such as the rate of activation? Tackling such questions requires new tools to acutely and
98 transiently perturb the Rho GTPase flux to understand its spatio-temporal regulation,
99 directly in single living cells. Note that this experimental paradigm was successful at
100 analyzing the Mitogen activated protein kinase (MAPK network) (Blum et al., 2019;
101 Dessauges et al., 2022; Ryu et al., 2015).

102 A promising candidate to investigate how mechanical feedback from FAs can spatio-
103 temporally shape Rho GTPase activity is the RhoA-specific GAP Deleted in Liver Cancer
104 1 (DLC1). DLC1 has been shown to both bind the PM (Erlmann et al., 2009), as well as
105 FAs (Haining et al., 2018; Kaushik et al., 2014). At the PM, interaction with
106 phosphatidylinositol-4,5-bisphosphate (PI(4,5)P2) can regulate GAP activity (Erlmann et
107 al., 2009). At the FA, DLC1 interacts with the r7-r8 domains of the FA protein talin in a
108 mechanosensitive fashion (Gingras et al., 2008; Goult et al., 2021; Haining et al., 2018;
109 Zhao et al., 2022), as well as with Focal adhesion kinase (Li et al., 2011). When talin is in
110 a state of low mechanical strain, it binds to DLC1 and presumably leads to local RhoA
111 inactivation. However, upon force application, the r7-r8 domains unfold leading to
112 dissociation of DLC1 from talin, leading to loss of negative RhoA regulation. This suggests

113 that DLC1 is regulated at FAs by mechanosensitive interactions, which can relay
114 information about the mechanical state of the cell to control RhoA activity.

115 In this work, we explore the spatio-temporal regulation of RhoA activity by DLC1. We show
116 that knocking out DLC1 in REF52 fibroblasts leads to increased amplitude in RhoA
117 throughout the cell. This is accompanied by an increased contractility that augments FAs
118 and stress fibers (SFs). To explore how DLC1 contributes to Rho GTPase activity fluxes,
119 we built a genetic circuit consisting of an optogenetic actuator to activate Rho with light,
120 and a spectrally compatible biosensor to measure Rho activity. Transient optogenetic
121 recruitment of a Rho GEF domain at FAs or at the PM led to an increase in the rate of
122 activation of Rho in *DLC1* KO versus WT cells at both subcellular localizations. However,
123 we found that in both control and DLC1 null cells, RhoA activation was more efficient at
124 FAs compared to the PM. Further, acute and local manipulation of contractility with the
125 optogenetic actuator revealed that DLC1 dynamically associates/dissociates with FAs
126 under acute mechanical tension/relaxation. Our results suggest a complex mechanism in
127 which DLC1-dependent Rho regulation can occur both at the PM and at FAs, with a
128 dependence on mechanosensitive signals on the latter.

129 Results

130 DLC1 deficient cells show increased formation of SFs and FAs

131 To investigate the function of DLC1 in cytoskeletal and adhesion dynamics, we knocked
132 down (KD) DLC1 in rat REF52 fibroblasts via small interfering RNA (siRNA). We also
133 created a knockout (KO) cell line via Crispr/Cas9, that has a frameshift deletion at position
134 841 of Exon 5 of the gene, resulting in an early in frame stop codon 100 bp downstream of
135 the cut. Gene-editing was validated by sequencing the endogenous locus. We were unable
136 to test expression levels using western blot because of the absence of commercially
137 available antibodies specific for rat DLC1. We then also rescued the *DLC1* KO cells with
138 an mCherry-labeled DLC1 construct using stable transfection with a piggyBac transposase
139 system. REF52 fibroblasts were seeded at subconfluent density onto fibronectin-coated
140 glass bottom wells and allowed to spread for one hour before fixation, leading to an
141 isotropic spreading state in control, wild-type (WT) cells. To assess the impact of DLC1
142 deficiency on the formation of cytoskeletal and adhesion structures, we stained for F-actin
143 (phalloidin) and paxillin (Figure 1A) or phospho-myosin light chain (pMLC) (Figure 1B).
144 Consistent with an expected increase in RhoA activity, we observed a phenotype of
145 increased contractility as documented by increased lamella size, SF content, number of
146 FAs, and increased pMLC. This increased contractility led to the loss of the isotropic
147 spreading observed in WT cells. Rescue with the DLC1 construct reverted the cells to a
148 less contractile phenotype that displayed a lamella of identical size as WT cells, enabling
149 the characteristic isotropic spreading observed in WT cells. Quantification of these images
150 revealed both an increase in lamella size (Figure 1C) and FA area (Figure 1D) in DLC1 KD

151 and KO cells versus WT and rescue cells (Figure1C). As previously documented in
152 fibroblasts (Kaushik et al., 2014), these results indicate that DLC1 feeds into the regulation
153 of contractility, SF and FA formation in fibroblasts. The less penetrant phenotype observed
154 in KO versus KD suggests that the KO cells might be able to adapt to the long-term absence
155 of DLC1, while KD cells had less than 48 hours to adjust to the new mechanical
156 state. These experiments also validate the *DLC1* KO cells and *DLC1* KO rescued with
157 mCherry-DLC1 that will be used in subsequent experiments.

158 **DLC1 deficient cells display altered spreading dynamics, lack of polarization**
159 **and efficient migration**

160 We timelapsed REF52 WT and *DLC1* KO cells for multiple hours in presence of platelet
161 derived growth factor (PDGF), a potent stimulator of fibroblast motility (Martin et al., 2014),
162 and evaluated their ability to migrate. We found that *DLC1* KO cells displayed a reduction
163 in both their speed of migration and their ability to migrate directionally (Figure S1A-C). We
164 then investigated cytoskeletal dynamics during spreading using REF52 fibroblasts stably
165 expressing the F-actin marker LifeAct (Riedl et al., 2008). Imaging early spreading (e.g. 20
166 minutes after plating) revealed no clear differences in edge dynamics in WT versus *DLC1*
167 KO cells (Figure 2A). However, kymograph analysis clearly showed that the lamella that
168 characteristically starts directly at the leading edge of the highly contractile REF52 cells
169 (Martin et al., 2016, 2014), was wider in *DLC1* KO versus WT cells. Later, 1 hour after
170 plating, when the cells are still spreading, lamellipodial protrusion/retraction cycles of wider
171 amplitude were observed in *DLC1* KO versus WT cells (Figure 2B, Movie S1), with again
172 a large increase in SF content (Figure 2B, right panel). After initial spreading, REF52
173 fibroblasts break their symmetry and eventually display short episodes of polarized cell
174 migration. Later, contractility builds up leading cells with spindle-like morphology. This
175 process occurs on timescales of multiple hours. To capture these behaviors, we
176 investigated cytoskeletal dynamics over the next 10 hours after reseeding at a slower
177 timescale that precludes observation of lamellipodial dynamics. While WT cells efficiently
178 broke their symmetry, and could display short stretches of polarized migration, *DLC1* KO
179 cells displayed robust stress fibers that hampered symmetry breaking and polarization
180 (Figure 2C, Movie S2). *DLC1* KO cells therefore rapidly adopted a spindle-like shape.
181 Quantification of the adoption of such a spindle shape phenotype showed that WT cells will
182 assume the spindle-like shape much later than *DLC1* KO cells and often fail to do so
183 entirely within the 10 hours of imaging (Figure 2D). Further highlighting a role for DLC1 in
184 RhoA-mediated control of contractility, we found that DLC1 overexpression leads to strong
185 reduction in the number of SFs (Figure S2A). Together, these results show that DLC1 loss
186 of function leads to increased contractility at the onset of spreading, which later impedes
187 polarization and directional cell migration.

188 **DLC1 deficient cells display an increase in global RhoA activity, without any**
189 **marked differences in RhoA activity pattern**

190 To explore how DLC1 spatio-temporally controls RhoA activity, we used RhoA2G (Fritz et
191 al., 2013), a fluorescence resonance energy transfer (FRET)-based biosensor that reports
192 on RhoA activity together with the Lifeact F-actin marker during spreading. As previously
193 observed (Martin et al., 2014), a RhoA activity band that correlates with the lamellar
194 contractile actomyosin network of the cell can be observed at the cell edge of WT REF52
195 fibroblast (Figure 3A, Movie S3). In *DLC1* KO cells, we observed global elevation of RhoA
196 activity throughout the cell. Quantification of both the average activity per cell and the local
197 edge RhoA activity revealed increased RhoA activity (Figure 3B). Kymograph analysis
198 revealed that the lamellar RhoA activity band remained of constant size during spreading
199 (Figure 3A). Examining cells approximately 10 hours after spreading when they had fully
200 spread, and WT cells had adopted a more contractile state, the DLC1 *KO* cells still exhibited
201 a global increase in RhoA activity (Figure 3C,D). This increase was however less strong
202 than in spreading cells, most likely because of a higher state of contractility in WT well-
203 spread versus spreading cells. We also evaluated the effect of overexpression of an
204 mCherry-tagged DLC1 on RhoA activity (Figure S2B). We observed that mild DLC1
205 expression, that remains mostly bound to FAs and to the PM and does not compromise
206 cell morphology, leads to a decrease in global RhoA activity. Strong DLC1 expression that
207 leads to a large cytosolic pool of DLC1 further diminishes global RhoA activity but then
208 compromises cell morphology. Together, these results suggest that DLC1 signaling at the
209 PM and at FAs controls global levels of RhoA activity within cells, rather than controlling
210 the spatio-temporal RhoA activity pool observed at the lamella.

211 **Design of an optogenetic actuator - Rho biosensor to interrogate the Rho**
212 **GTPase flux**

213 While FRET measurements as shown above provide insight about a steady-state RhoA
214 activity pattern, they cannot probe in detail how a GEF/GAP/GTPase signaling network
215 might affect the Rho GTPase flux which most likely emerges from the regulation of multiple
216 GEFs and GAPs. For example, GAP-mediated negative regulation might control Rho
217 GTPase signal duration, but might also be involved in adjusting the rate of activation. We
218 reasoned that transient, acute optogenetic perturbations of the Rho GTPase flux, followed
219 by measuring Rho activity dynamics might provide new insights about its regulation. To
220 manipulate Rho activity in single living cells, we re-engineered an iLID-based optogenetic
221 actuator based on a DH/PH domain of the GEF LARG (Oakes et al., 2017) (Figure 4A). We
222 used a high affinity nano SspB domain for efficient light-dependent recruitment of the LARG
223 GEF domain to the iLID anchor. To better focus optogenetic activation, we also fused the
224 iLID anchor to a stargazin membrane anchor that slows down its diffusion (Natwick and
225 Collins, 2021). Both the stargazin-iLID anchor and the SspB-LARG domains were

226 separated by a P2A self-cleaving peptide, allowing for equimolar expression of both units
227 from a single operon. We refer to this construct as optoLARG. To interrogate the Rho
228 GTPase flux, we engineered a REF52 line that stably expressed the optogenetic construct
229 as well as a rhotekin-based G protein binding domain (rGBD) that reports on Rho activation
230 (Mahlandt et al., 2021). The rGBD probe is labelled with a tandem dimeric Tomato
231 (tdTomato) fluorophore that is spectrally orthogonal to optogenetic activation. We used a
232 truncated CMV promoter to warrant low expression level of the rGBD probe to avoid
233 dominant negative effects of the construct through inhibition of Rho signaling. We also
234 expressed a spectrally orthogonal far-red Lifeact-miRFP construct that reports on F-actin
235 dynamics. Because rGBD cannot distinguish between the activity of the RhoA, RhoB and
236 RhoC isoforms, we refer to any rGBD measurement as Rho activity. This is in marked
237 contrast with RhoA2G, the FRET biosensor we used above that is specific for RhoA (Fritz
238 et al., 2013), but is not spectrally compatible with optoLARG. Note that both biosensors are
239 able to measure active Rho GTPase pools during robust morphogenetic events such as
240 tail retraction (Fritz et al., 2013; Mahlandt et al., 2021), while rGBD misses leading edge
241 Rho GTPase activity pools widely observed using FRET probes (Machacek et al., 2009;
242 Martin et al., 2016; Pertz et al., 2006).

243 We then used a digital micromirror device (DMD) to spatially shine repetitive pulses of blue
244 light delivered at different frequencies on 2 distinct regions of interest (ROIs) at the edge
245 of fibroblasts. When light pulses were delivered at high frequency, we observed robust Rho
246 activation at the edge, which correlated with assembly of contractile F-actin structures and
247 potent edge retraction (Figure 4B, kymograph shown in 4C, Movie S4). Removal of the
248 blue light pulses led to a subsequent decrease in Rho activity, and reversion of the edge
249 to a protrusive state. Further, stimulating a ROI at the opposite edge of the cell with a lower
250 light pulse frequency led to a lower Rho activation, and less robust edge retraction. These
251 results indicate that depending on the strength of the light input, optoLARG can locally,
252 reversibly, and quantitatively control Rho activity in single living cells on timescales of
253 seconds, allowing us to acutely manipulate the Rho GTPase flux.

254 **Optogenetic interrogation of the Rho GTPase flux in WT and *DLC1* KO cells**

255 Because DLC1 might both regulate the Rho GTPase flux both at the PM (Erlmann et al.,
256 2009) and at FAs (Haining et al., 2018), we performed a series of experiments using
257 optoLARG to transiently activate RhoA with the expectation of observing different
258 perturbations in Rho activity fluxes in control versus *DLC1* KO cells. For that purpose, we
259 produced WT and *DLC1* KO REF52 lines expressing optoLARG, the tdTomato-rGBD
260 biosensor and miRFP-paxillin as a readout for FAs. We first sought to locally activate RhoA
261 by illuminating large ROIs at edges and evaluate any difference in Rho activity patterns
262 using the spectrally compatible rGBD biosensor in WT versus *DLC1* KO cells. We however
263 were not able to identify a threshold optogenetic light input that would induce different RhoA
264 activity patterns and edge dynamics in WT versus the more contractile *DLC1* KO cells. We

265 observed that the same light input could induce edge retraction in both WT and *DLC1* KO
266 cells in a non-predictable manner. This might be due to the spatial heterogeneity of the
267 mechanical states within cells, as well as small differences in optoLARG and rGBD
268 expression levels in the stable cell lines. To address this caveat, we reasoned that we
269 should activate Rho using optoLARG with a more subtle modality by illuminating only small
270 ROIs and measuring small local fluctuations of Rho activity using rGBD without inducing
271 large changes in mechanical states. Further, to dissect potential regulation of *DLC1* GAP
272 activity by PI(4,5)P2 at the PM (Erlmann et al., 2009) versus mechanosensitive interactions
273 at the FA (Haining et al., 2018), we decided to make measurements on FAs but use ROIs
274 outside of FAs (non-FAs ROIs) to probe the PM. For that purpose, we built an image
275 analysis pipeline to first segment a cell in a field of view and to then segment FAs based
276 on their fluorescent intensity, size and localization at the cell periphery using the paxillin-
277 miRFP signal (Figure 5A). We then used these FA segmentations to illuminate small ROIs
278 within FAs or in neighboring non-FA ROIs with one pulse of blue light using the DMD and
279 evaluated rGBD fluorescence fluctuations at this location for a couple of minutes until Rho
280 activity returned to baseline (Figure 5B). This optogenetic stimulation had no visible effect
281 on edge retraction, or FA morphodynamics, as observed when stimulating larger ROIs.
282 Quality control of our automated segmentation revealed high versus low paxillin signals in
283 FA versus non-FA ROIs (Figure 5C). This experiment was performed on multiple cells,
284 allowing to average out any experimental noise due to small differences in expression
285 levels of optoLARG or rGBD. These data were then averaged for FA and non-FA ROIs.
286 We observed that this pulsed optoLARG light input led to a local transient of Rho activity
287 for approximately 2.5 minutes in WT cells when FAs or the PM were stimulated (Figure
288 5D). To quantify observed activation ($k_{\mathrm{ON}}^{\mathrm{obs.}}$) and deactivation ($k_{\mathrm{OFF}}^{\mathrm{obs.}}$) rates, we defined a 10-
289 90% time window of the activation and deactivation phases and computed the mean
290 derivative over each window. The identical optoLARG input led to an increased observed
291 rate of Rho activation leading to higher amplitude when an FA versus a non-FA ROI was
292 stimulated ($k_{\mathrm{ON}}^{\mathrm{obs.}}$: 0.0132 (non-FA) < 0.0176 (FA)). In *DLC1* KO cells, we observed
293 increased Rho activation rate that also led to augmented Rho activity amplitude in
294 comparison with WT cells in both FA and non-FA ROIs ($k_{\mathrm{ON}}^{\mathrm{obs.}}$: 0.0195 (non-FA) < 0.0221
295 (FA)). This was also accompanied with faster deactivation kinetics of RhoA ($k_{\mathrm{OFF}}^{\mathrm{obs.}}$: 0.0060
296 (non-FA KO) < 0.0068 (FA KO), $k_{\mathrm{OFF}}^{\mathrm{obs.}}$: 0.0042 (non-FA WT) < 0.0054 (FA WT)). These data
297 suggest that under weak transient GEF input, DLC1 regulates the rate of Rho activation
298 and peak amplitude rather than signal duration. Note that $k_{\mathrm{ON}}^{\mathrm{obs.}}$ and $k_{\mathrm{OFF}}^{\mathrm{obs.}}$ here refer to the
299 rates observed in the biosensor signal, which reflect the combined effects of underlying
300 activation and deactivation processes rather than parameters of GEF/GAP activity. This
301 can occur both at the PM and at FAs. The finding that *DLC1* KO also leads to faster
302 deactivation suggests the existence of compensatory negative feedback that points to
303 complex modalities of spatio-temporal regulation that most likely involves additional
304 GEFs/GAPs. In both WT and *DLC1* KO cell lines, RhoA activation rates and peak levels

305 were higher at FAs than in non-FA regions. To exclude that this difference could be an
306 artefact from differential recruitment of the optogenetic tool, we directly measured
307 optoLARG localization using a cell line expressing mScarlet3-optoLARG and miRFP-
308 paxillin, which allowed imaging of optoLARG recruitment without activation. We repeated
309 the experiment from Figure 5, this time quantifying optoLARG intensity instead of RhoA
310 activity, and found no significant difference in recruitment kinetics between FAs and non-
311 FAs (Figure S3A,B), excluding tool recruitment as a confounding factor. These results
312 instead suggest that FAs provide a subcellular environment that favors GEF-mediated
313 activation of Rho activity compared to non-FA regions. The recruitment and dissociation
314 dynamics of optoLARG were well described by an inverse exponential function during
315 association and an exponential decay function during dissociation (Figure S3C). The
316 measured deactivation half-life was 10.8 s, which is faster than previously reported values
317 2016) (t½ OFF = 18 ± 2 s in vitro; 32.0 ± 3.7 s for membrane localization in cells) (Hallett
318 et al.). Our experimental design differs from previous reports in that activation was
319 restricted to small regions of the cell, whereas prior studies used whole-cell illumination.
320 The accelerated decay we observed may therefor result from additional diffusion of
321 optoLARG out of the locally stimulated regions.

322 The experimental data revealed distinct activation and deactivation kinetics between WT
323 and *DLC1* KO cells, suggesting altered regulatory feedback within the RhoA signaling
324 network. We next sought to investigate the mechanistic basis of these differences by
325 mathematical modeling.

326 **Modeling suggests loss of negative RhoA autoregulation in *DLC1* KO cells**

327 To quantitatively describe the regulatory dynamics of RhoA signaling following transient,
328 localized optogenetic stimulation at FAs and the PM in WT and *DLC1* KO cell lines, we
329 constructed a system of ordinary differential equations (scheme in Figure 6A). This
330 modeling framework allows us to disentangle the underlying activation and deactivation
331 rates from the apparent rates observed with the biosensor and infer qualitative regulatory
332 differences between WT and KO cells. The experimental measurements of optoLARG
333 recruitment were first used to fit a simple linear model of protein activation and deactivation,
334 enabling estimation of the kinetic parameters governing optoLARG dynamics. Based on
335 this fit, the active GEF profile (GEF^*) was treated as a fixed, time-dependent input to the
336 downstream model of RhoA activity. The remaining regulatory interactions, including RhoA
337 activation by GEFs, RhoA inactivation by GAPs, and RhoA-dependent GAP activation, are
338 captured in the following system using loosely constrained parameters:

339 $$\frac{d\mathrm{LARG}^*}{dt} \approx k_{\mathrm{on}}^{\mathrm{LARG}} \cdot f_{\mathrm{signal}}(t) - k_{\mathrm{off}}^{\mathrm{LARG}} \cdot \mathrm{LARG}^*$$

340 $$\frac{d\mathrm{GAP}^*}{dt} \approx \frac{V_{\mathrm{on}}^{\mathrm{GAP}} \cdot \mathrm{Rho}^*}{Km^{\mathrm{GAP}} + \mathrm{Rho}^*} - k_{\mathrm{off}}^{\mathrm{GAP}} \cdot \mathrm{GAP}^*$$

$$\frac{d\mathrm{Rho}^*}{dt} \approx \frac{V_{\mathrm{on}}^{\mathrm{Rho}} \cdot \mathrm{LARG}^*}{Km_{\mathrm{on}}^{\mathrm{Rho}} + \mathrm{LARG}^*} - \frac{V_{\mathrm{off}}^{\mathrm{Rho}} \cdot \mathrm{GAP}^* \cdot \mathrm{Rho}^*}{Km_{\mathrm{on}}^{\mathrm{Rho}} + \mathrm{Rho}^*}$$

$$k_{\mathrm{on}}^{\mathrm{LARG}} = 0.0123462$$

$$k_{\mathrm{off}}^{\mathrm{LARG}} = 0.0700499$$

Michaelis-Menten kinetics were used to model RhoA activation by active optoLARG (LARG^*), inactivation by active GAPs (GAP^*), and a RhoA-dependent feedback on GAP activation (Rho^*) (De Seze et al., 2023). GAP inactivation was approximated as a first-order process. Given the transient and low-amplitude nature of the optogenetic stimulus, we assumed that the inactive forms of optoLARG, GAP, and Rho remained in large excess throughout the simulation. This allowed us to simplify the model by treating the concentrations of the inactive species as effectively constant over time. The resulting system of ODEs was solved and fitted to the experimental data using gradient-based optimization in Julia (Figure 6B,C). We additionally assessed the structural identifiability of all parameters. Full implementation details and the results of the structural identifiability analysis are provided in the Methods section.

In WT cells, the model provides a strong fit to the experimental data and supports the use of canonical Michaelis-Menten kinetics for RhoA activation and inactivation, as well as the negative feedback on GAP. The results indicate that RhoA activity is dynamically regulated by active GAPs, which are themselves activated by RhoA, forming a negative feedback loop. This feedback ensures that RhoA activation remains transient and self-limiting. The fitted parameters reflect saturable enzyme-substrate interactions, consistent with standard biochemical expectations.

In contrast, the behavior observed in *DLC1* KO cells reveals a disruption of this feedback mechanism. When fitted with the same model structure, the parameter for RhoA-dependent GAP activation converges to zero, indicating loss of negative feedback. Instead, the system appears to rely on a constitutively active or pre-localized GAP-like component that inactivates RhoA at a fixed rate. This configuration eliminates feedback modulation and produces RhoA dynamics that are governed by constitutive GAP activity, possibly due to the global GAP activity of multiple RhoA-specific GAPs in the cell.

A limitation we encountered in our modeling is that the fitted parameter magnitudes happened to depend on the bounds imposed during optimization. Structural identifiability analysis confirmed that all parameters are theoretically globally identifiable given the model structure and observables. Yet in practice, some fitted values were found to vary with the parameter bounds chosen. While some parameters (e.g., responsible for RhoA activation or RhoA-dependent GAP activation) were robust across fits, others varied without significantly affecting model performance. This reflects the distinction between structural and practical identifiability (Gutenkunst et al., 2007; Lam et al., 2022) where the robustness

377 and uniqueness of fitted parameter can be limited by the experimental data. We therefore
378 limited our attention on qualitative differences in regulation (feedback present vs. absent),
379 rather than absolute numerical parameter values.

380 **DLC1 differently interact with FAs depending on their mechanical states**

381 Our finding that we did not observe striking patterns of RhoA activity in the vicinity of FAs
382 in spread cells challenges the idea that mechanical inputs regulate Rho activity in this
383 specific regime of mechanical forces. We speculated that the DLC1/talin system in FAs is
384 only mechanosensitive to stronger mechanical inputs. To evaluate FA-DLC1 interactions,
385 we imaged fibroblasts rescued with mCherry-DLC1 and miRFP-paxillin as a marker for
386 FAs. We observed that DLC1 binds to FAs at the onset of FA assembly, and that the local
387 DLC1 density augmented with the paxillin density (Figure S4A-C). During FA disassembly,
388 DLC1 density diminished concomitantly with decreasing paxillin density until the FA was
389 fully disassembled (Figure S4D-F).

390 To characterize force-dependent interactions of FAs with DLC1 in regimes of strong
391 mechanical perturbations, we engineered our mCherry-*DLC1* rescue cells to stably express
392 the optoLARG system, as well as the miRFP-paxillin construct. We then used the DMD to
393 activate Rho-mediated contractility locally and transiently in small ROIs containing FAs with
394 a standardized light input. The transient light pulse induced either of the two FA behaviors:
395 light-mediated FA reinforcement as evidenced by a local increase in paxillin density, was
396 followed by 1. FA relaxation (and decrease in paxillin density) upon light removal (Figure
397 7A-C, quantified in Figure 7D, Movie S5), or 2. FA rupture (Figure S5A-C). This was
398 accompanied by a striking simultaneous decrease in DLC1 intensity at the FA during FA
399 reinforcement, and a reassociation of DLC1 during FA relaxation upon light input removal.
400 If the light input led to FA rupture, then the DLC1 signal gradually decreased along FA
401 reinforcement until the FA ultimately ruptured in an all-or-nothing manner. FAs in the same
402 cell that were not subjected to the light input displayed dynamics as in normal cells, as
403 shown in Figure 7 (Figure S5D-F). These results indicate that DLC1 dynamically
404 dissociates and associates during acute FA reinforcement and relaxation in response to a
405 strong mechanical input.

406 Discussion

407 A key question in Rho GTPase biology is how multiple GEFs and GAPs control spatio-
408 temporal Rho GTPase signaling patterns to regulate cytoskeletal dynamics that power
409 morphogenetic processes such as cell migration. The recent finding that many GEFs and
410 GAPs themselves bind cytoskeletal and adhesion structures (Müller et al., 2020) strongly
411 suggests direct feedback from the cytoskeleton to Rho GTPase signaling. Self-
412 organizational properties of cytoskeletal and adhesions structures might therefore
413 contribute to spatio-temporal control of Rho GTPase signaling. Because DLC1 has been

414 proposed to bind to FAs in a mechanosensitive manner (Haining et al., 2018), we decided
415 to study it as a prototypical example of an adhesion feedback to Rho GTPase signaling.
416 Using novel technologies that allow for acute spatio-temporal perturbations, we provide
417 some new insights about how Rho GTPases are spatio-temporally controlled by a RhoGAP
418 that integrates mechanosensitive inputs.

419 We found that in spreading fibroblasts, *DLC1* KO globally augments contractility, as
420 illustrated by a robust increase in SFs and FAs (Figure 1). Evaluation of F-actin dynamics
421 immediately after spreading, when global contractility levels are still low, reveal that *DLC1*
422 KO fibroblasts rapidly assemble a wider contractile lamella than WT cells, suggesting
423 aberrant increase of myosin-based contractility already at an early stage of spreading
424 (Figure 2A). One hour after cell plating, when cells are well spread but still retain an
425 isotropic shape, we observed a global increase in contractility in *DLC1* KO versus WT cells
426 (Figure 3B). On a timescale of multiple hours after spreading, when WT cells break
427 symmetry, display polarized cell migration episodes, and finally adopt a contractile state
428 leading to a spindle morphology, we find that *DLC1* KO cells transition directly to the
429 contractile phenotype without being able to polarize (Figure 2C,D). Thus, DLC1 loss of
430 function leads to a global increase of aberrant contractility.

431 We had previously shown that REF52 fibroblasts display a wide band of RhoA activity that
432 correlates with the lamellar contractile myosin network during spreading (Martin et al.,
433 2016, 2014). We found that *DLC1* KO leads to a global increase in RhoA activity throughout
434 the cell, without however markedly modifying the spatial band of RhoA activity at the
435 lamellum (Figure 3A,B). Similar results were observed when cells were allowed to further
436 polarize and assemble a robust actomyosin cytoskeleton (Figure 3C,D). Further, we
437 observed that mild DLC1 expression, that can still mostly be titrated by FAs and the PM
438 without spilling out into the cytosol, is already able to strongly downregulate global RhoA
439 activity levels (Figure S2B). These findings suggest that in spread cells, DLC1 mainly sets
440 the overall baseline of RhoA activity, while the spatial distribution of RhoA activation, such
441 as observed at the lamellar band observed in spreading cells, appears to be maintained by
442 other, spatially restricted GEFs/GAPs that control localized RhoA pools at protrusive edges
443 and filopodia (Fritz and Pertz, 2016b; Machacek et al., 2009; Pertz et al., 2006), within the
444 lamella (Martin et al., 2016, 2014). Similarly, additional GEFs/GAPs might be specifically
445 spatio-temporally regulating the cytokinetic furrow (Basant and Glotzer, 2018; Bement et
446 al., 2015). Note that the classic genetic perturbation paradigm is only of limited value to
447 study the dynamic regulation of Rho by DLC1 at FAs because long-term loss of DLC1
448 function results in cells being locked in a state of excessive contractility.

449 To address this question, we used optogenetic control of Rho activation to probe different
450 aspects of DLC1-mediated regulation of Rho activity at FAs, sites where DLC1 is highly
451 enriched (Figure 7), and regulates Rho through talin- and tensin-dependent interactions,
452 as well as at control regions on the PM, where DLC1 can bind lipids but is less abundant

453 (Erlmann et al., 2009; Haining et al., 2018). In a first experimental modality, we evaluated
454 the Rho activity flux at FAs as well as the PM in a mechanical regime that does not involve
455 FA reinforcement (Figure 5). In the 2nd experimental modality, we evaluated force-
456 dependent DLC1-FA interaction in a mechanical regime in which FA reinforcement is
457 clearly occurring (Figure 5).

458 In the first experimental modality, we probed the Rho GTPase flux under conditions that
459 did not trigger FA reinforcement (Figure 5D). The goal was to probe DLC1-dependent
460 regulation of Rho in absence of strong mechanical strain. To achieve this, we applied small
461 light inputs that induced only subtle fluctuations in Rho activity. Due to the weak signal-to-
462 noise ratio (SNR) of these subtle GEF inputs, meaningful measurements of Rho activity
463 response dynamics could only be obtained by averaging signals across hundreds of FAs.
464 We observed that a transient synthetic optoLARG input applied to a FA yielded a Rho
465 activation transient indicating the presence of tonic Rho GAP activity in the cell (Figure
466 5E,F). Interestingly, we observed that the identical synthetic optoLARG input applied to the
467 PM in absence of FA led to a Rho activity transient of lower amplitude. This suggests that
468 FAs are intrinsically more permissive for GEF-mediated Rho activation, potentially due to
469 local Src-dependent release of Rho from RhoGDI (DerMardirossian et al., 2006).

470 Since Rho activity may be regulated by DLC1 at FAs, we initially expected to observe
471 altered Rho dynamics at these sites in *DLC1* KO cells, specifically that transient optoLARG
472 input would lead to prolonged Rho activity. We found however that RhoA activation
473 occurred faster, reached a higher peak amplitude, and returned to baseline more rapidly in
474 both FA and non-FA PM regions compared to control cells (Figure 5E,F). Given that DLC1
475 is strongly enriched at FAs relative to the PM, the observation that similar RhoA flux
476 changes occur at both subcellular locations suggests that these effects do not arise solely
477 from local DLC1 activity. Rather, they may also reflect compensatory expression or
478 activation of other GEFs and GAPs triggered by DLC1 loss. This interpretation is consistent
479 with our experimental observation that *DLC1* KO cells engage compensatory mechanisms
480 over time, resulting in weaker phenotypic differences than those observed in acute
481 knockdown (Figure 1). However, such compensation likely lacks spatial specificity, as it
482 does not adapt to local RhoA concentrations. This behavior mirrors findings in T cells,
483 where Cdc42 deletion triggered compensatory transcriptional programs that restored
484 cellular function (Rochussen et al., 2025), illustrating how Rho GTPase networks can
485 rapidly adapt to gene loss and thereby mask the impact of individual regulators.

486 Our mechanistic model of dynamic RhoA modulation, fitted to experimental measurements
487 of GEF input and resulting RhoA activity, further supports this view. The model revealed
488 qualitative differences between WT and *DLC1* KO cells: WT cells exhibited Rho-dependent
489 negative feedback that dampens activation dynamics, whereas this feedback was lost in
490 the KO condition. The absence of this negative autoregulation explains the higher Rho
491 activation amplitude observed in KO cells and implies that, in the absence of DLC1,

492 alternative Rho-regulated GAPs or regulatory proteins act independently of RhoA levels.
493 Such negative feedback architectures are a hallmark of small GTPase signaling networks
494 (Bement et al., 2024; Tsyganov et al., 2012; Wu and Lew, 2013), where they confer
495 robustness and dynamic stability to signaling outputs. Altogether, our results uncover an
496 unexpected complexity in the spatiotemporal regulation of Rho GTPase signaling at FAs,
497 likely involving multiple GEFs and GAPs. They also highlight how long-term genetic
498 perturbations can activate compensatory mechanisms, complicating the interpretation of
499 single-gene knockouts. Future experiments will require high-resolution, dynamic
500 measurements of multiple GEFs, GAPs, and RhoA activity in unperturbed cells, or
501 alternatively, acute perturbations that precede the onset of compensatory responses.

502 In the second experimental modality, we investigated mechanosensitive interactions
503 between FAs and DLC1 under optoLARG stimulation conditions that promote robust FA
504 reinforcement. We transiently increased actomyosin contractility within a small ROI, which
505 triggered FA reinforcement followed by relaxation (Figure 7). Under such acute mechanical
506 perturbations, we observed distinct DLC1 dynamics at FAs, likely involving its known
507 mechanosensitive interactions with talin (Haining et al., 2018). In response to the induced
508 strain, DLC1 rapidly dissociated from FAs exhibiting strong reinforcement (Figure 7;
509 schematic in Figure 7F). This behavior correlates with in vitro findings showing that DLC1
510 dissociates from stretched talin due to unfolding of its R7-R8 domain (Haining et al., 2018).
511 We also observed that FA relaxation promotes re-binding of DLC1 to FAs (Figure 7),
512 suggesting that the R7-R8 talin domain might refold in these conditions. In this context,
513 strong local mechanical input leading to FA reinforcement and talin stretching may cause
514 rapid unbinding of DLC1 from FAs, transiently reducing local RhoGAP activity and
515 providing a positive feedback loop that increases RhoA activation and local contractility.
516 This may, in turn, promote FA disassembly as observed experimentally. Conversely, when
517 the mechanical input ceases, DLC1 re-binding to relaxing FAs may rapidly suppress RhoA
518 activity, restoring a low-contractility steady state. These nonlinear feedback mechanisms
519 may enable amplification of local mechanical inputs to regulate all-or-nothing cytoskeletal
520 events such as tail retraction during migration. Tail retraction is characterized by brief bursts
521 of localized RhoA activity followed by rapid relaxation once retraction is complete (Martin
522 et al., 2014; Pertz et al., 2006). In this model, stress fiber pulling on FAs at the cell rear
523 could trigger local DLC1 release, transiently elevate RhoA activity, and drive strong
524 localized contraction leading to tail retraction. Testing this hypothesis experimentally is
525 challenging, as long-term DLC1 perturbation will induce global hypercontractility,
526 preventing cell polarization, directional migration and thus the production of tail retraction
527 events.

528 Summarizing the results from these two experimental regimes, we propose that DLC1
529 provides two distinct levels of Rho regulation. Under low mechanical input, DLC1 may help
530 control global RhoA activity by positioning localized hotspots of RhoGAP activity throughout

531 the cell, most likely together with other Rho GAPs. In contrast, under strong mechanical
532 input leading to FA reinforcement, the DLC1-talin mechanosensitive interaction may permit
533 rapid, local positive feedback on RhoA activity through DLC1 dissociation from FAs. This
534 positive feedback could enable efficient FA turnover in response to mechanical stimuli and
535 regulate processes such as tail retraction.

536 Our results illustrate how spatially controlled optogenetics with optoLARG enables
537 spatiotemporal, reversible control of contractility, revealing mechanosensitive signaling
538 interactions that are otherwise obscured by classical global perturbations of RhoA, such as
539 nocodazole-induced microtubule depolymerization (Krendel et al., 2002) or
540 lysophosphatidic acid-mediated RhoA activation (Pertz et al., 2006) which trigger broad
541 and nonspecific contractile responses. These findings provide new insight into the network
542 circuitry governing spatiotemporal Rho GTPase signaling and point toward a new
543 experimental modality for dissecting these mechanisms. By combining precise, reversible,
544 and spatially confined optogenetic perturbations with automated optogenetic targeting, we
545 can now locally modulate Rho activity and probe signaling fluxes across different regimes,
546 using gentle perturbations to nudge the system out of equilibrium and reveal its relaxation
547 back to steady state, or stronger inputs to engage mechanical feedback and adhesion
548 reinforcement. Although this study focused on a GAP localized to FAs, the same approach
549 can be extended to other cytoskeletal structures by targeting actin, myosin, or microtubule
550 markers to guide light stimulation in real time. Such strategies will allow systematic mapping
551 of how localized biochemical and mechanical feedback, mediated by multiple GEFs and
552 GAPs, combine to generate emergent signaling patterns. Future studies systematically
553 perturbing individual and combined GEFs and GAPs under controlled optogenetic
554 stimulation will be essential to identify their specific contributions to Rho GTPase flux and
555 feedback architecture. Ultimately, achieving this level of quantitative, structure-specific
556 control will be key to understanding how dynamic Rho GTPase signaling under the control
557 of multiple GEFs and GAPs orchestrates cell morphogenesis.

558 Materials and methods

559 **Cell culture**

560 Rat Embryo Fibroblast 52 (REF52) were cultured in Dubelcco's Modified Eagle Medium
561 with 4.5 g/l glucose, 10% 4mM L-Glutamine, and 100 U/ml penicillin/streptomycin. Cells
562 were grown at 37 ºC and 5% CO2.

563

564 **SiRNA knockdown**

565 4µl lipofectamine RNAi max was mixed with a total of 500µl of OPTIMEM medium and a
566 pool of SiRNAs against the gene of interest at a final concentration of 60 nM (SiTools

567 Biotech). The mix was added to a 6 well plate containing 100000 cells in a 2 ml medium
568 volume medium.

569

570 **CrispR/Cas9 Knockout generation**

571 Two guide sequences targeting DNA within exon 5 of the DLC1 gene were selected using
572 the CRISPOR tool for predicted high-specificity protospacer adjacent motif target sites in
573 the rat genome [32] . Two complementary oligos each containing the DLC1 guide sequence
574 and BbsI ligation adapters were synthesized (Microsynth) (sense sequence: 5'-
575 CACCGAACCGAGAGAGCTACCCGG-3', antisense sequence: 5'-
576 AAACCCGGGTAGCTCTCTCGGTTC-3'). The guide sequences were annealed and
577 ligated into a pSpCas9(BB)-2A-GFP vector. REF52 cells were grown in six-well plates to
578 60% confluency and transfected with 1µg of the vector together with 1 µl of Lipofectamine
579 3000 and 5 µl of P3000 solution (ThermoFisher Scientific). Two days post transfection cells
580 were detached, suspended in PBS +1% FBS and sorted into 96 well-plates using
581 fluorescence-activated cell sorting. After expansion, individual clones were detached and
582 suspended in the lysis buffer (10mM TRIS, 50mM KCL, 2.5mM MgCl2, 0.45% Tween-20,
583 0.05% Gelatine, 0.12 mg/ml of proteinase K). The cell solution was frozen at -80 °C and
584 subsequently kept at 63 °C for one hour. Proteinase K was inactivated by heating the
585 solution to 95 °C for 15 minutes. PCR primers were designed to amplify a 500bp region
586 around the CRISPR cut site (forward primer: 5'-
587 AAGGAGTGTGTCTAACTCCACGCAGACCAG-3', reverse primer: 5'-
588 CTCCTTAGGACTGTCGCTGCTGTTTTCTCT-3'). Genomic sequences were amplified by
589 PCR and sequenced by Sanger sequencing.

590

591 **DNA constructs**

592 A "pB3.0" piggybac vector was created by adapting the pPBbsr2 (Matasci et al., 2011) to
593 make it smaller in size. pPBbsr2 was digested with AscI and PacI, yielding 3922 bp and
594 2864 bp fragments. Full size pPBbsr2 was used as template for a PCR with forward primer
595 5'-TTAGCATTAATTAAGCGGCCGCGTTGCTGGCGTTTTTCC-3' and reverse primer 5'-
596 GTGCCTTTACAACTTATGAGTAACCCCGCGCGGACGATT-3', yielding a 1671bp insert
597 that was ligated back into the receiving 3922bp part of the digested pPBbsr2 vector,
598 creating "pB3.0-BLAST" (Blasticidine resistance). To introduce different resistance
599 cassettes, we performed an overlap extension PCR with pB3.0-BLAST as template for
600 PCR1 (primers A+B) and PCR2 (primers C+D) with the following primers:

601 primer A: 5'-AAGGATGCCCAGAAGGTACCCCATTGTATGGGATCTGATCTGGG-3',
602 primer B: 5'-GGAAACTTTTTGTGCTATTATGGTGGCCATTCAGCTCTACGTAGCTACT-

603 3', primer C 5'-
604 CCTTTGAAAAACACGATAATACCACCGGTAAGTCGAGATGCATCGATGA-3', primer D:
605 5'-CTCCGCCTTTCTTGGACGTCGGGTTCGAACCGCATTAGT-3'. Primers A and D, the
606 product of PCR1 and PCR2 were used for fusing the two fragments by PCR. The resulting
607 PCR product was ligated into the pB3.0-BLAST vector, digested with Kpn1 and Pst1, by
608 fusion cloning, yielding a pB3.0-noAB vector with a single Age1 site to introduce antibiotic
609 resistance cassettes. To produce pB3.0-HYGRO and pB3.0-PURO, PCRs were performed
610 on template vectors pHygro-PB and pPuro-PB, respectively. For pB3.0-HYGRO forward
611 primer 5'-AACACGATAATACCACCATGAAAAAGCCTGAACTCACCGC-3' and reverse
612 primer
613 5'-GCAGGCTCCCGTTTCCTTATCGGCCATTCAGCTCTA-3' were used. For pB3.0-
614 PURO forward primer 5'-AACACGATAATACCACCATGACCGAGTACAAGCCCACG-3'
615 and reverse primer 5'-GCGTTCGGGCCACGGACTGGCCATTCAGCTCTA-3' were used.
616 The respective inserts were inserted via fusion cloning in the pB3.0-noAB vector [33],
617 digested with AgeI.

618 Construction of the pB3.0-optoLARG-mVenus-SspB-p2A-stargazin-mtq2-iLID optoLARG
619 system was as follows. The cDNA for optoLARG-mVenus-SspB(nano)-p2A-iLID-CAAX
620 was synthesized by custom gene synthesis (Genewiz, Azenta life sciences, US). The
621 sequence contained the catalytical DH-PH domain of human RhoGEF12 (LARG, aa 766-
622 1138), connected via a linker (GSGSGSGS) to full-length mVenus fused to SSPB(nano).
623 This is followed by a p2A sequence (GSGATNFSLLKQAGDVEENPGP), the iLID module
624 (Guntas et al., 2015) and a CAAX box (KRAS). The construct was cloned into pB3.0-BLAST
625 containing a CAG promotor, yielding pB3.0-optoLARG-mVenus-SspB-p2A-iLID-CAAX.
626 After publication of an improved PM anchor for the iLID-module (Natwick and Collins,
627 2021), we changed the part after the p2A sequence. The pB3.0-optoLARG-mVenus-SspB-
628 p2A-iLID-CAAX vector was digested with BsrGI and AflII, and a custom gene synthesized
629 stretch of cDNA containing SspB(nano)-p2A, full-length stargazin, mTurqoise2 and iLID
630 was inserted. This yielded pB3.0-optoLARG-mVenus-SspB(nano)-p2A-stargazin-mtq2-
631 iLID (exact sequences of the gene synthesis products are available on request). We also
632 developed a version with the recruitable SSpB domain tagged in red (mScarlet3) instead
633 of yellow (mVenus), which allowed to image optoLARG recruitment without activating it.

634 An eGFP DLC1 plasmid containing the 1091aa long isoform originating from mouse (kindly
635 provided by Monilola A. Olayioye) was used to produce mCherry-DLC1. The DLC1 gene
636 was cut out of this plasmid with BamHI and, N-terminally fused to FKBP12-mCherry and
637 inserted into pB3.0-BLAST containing a CAG-promotor, yielding pB3.0-FKBP12-mCherry-
638 DLC1.

639

640 **Spreading Assay**

641 Glass bottom well plates (Celvis) were coated with 5 µg/ml of human plasma fibronectin
642 purified protein (Merck) for one hour at room temperature. REF52 cells were seeded at a
643 density of 7000 cells per well (using 24 well plates) in FluoroBrite DMEM medium
644 containing 1% FBS, 0.1% BSA, 4mM L-Glutamine and 100 U/ml penicillin/streptomycin.
645 Imaging was done with a Nikon Eclipse Ti-E inverted microscope with an automatic stage.
646 Temperature was kept at 37ºC with a temperature control system, humidity (100%) and
647 CO2 (~5%) with a gas mixer (Life Imaging Services). Focus drift was prevented by the
648 equipped Perfect Focus System (Nikon). The microscope was controlled with Metamorph
649 software (Universal Imaging).

650

651 **Optogenetic Stimulation experiments**

652 Glass bottom well plates (Celvis) were coated with 5 µg/ml of human plasma fibronectin
653 purified protein (Merck) for one hour at room temperature. REF52 cells were seeded at
654 6000 cells/well into 12 well plates and allowed to attach for 12 hours. For both RhoA activity
655 and mCherry-DLC1/miRFP-paxillin optogenetic stimulation experiments cells were
656 incubated in FluoroBrite DMEM medium overnight. The microscope was controlled with
657 NIS-Elements (Nikon) for observing DLC1 dynamics and with open-source micromanager
658 software (Edelstein et al., 2014) for edge stimulation. Optogenetic stimulation was localized
659 to specific regions using an Andor mosaic 3 DMD. For mCherry-DLC1/miRFP-paxillin
660 experiments, ROIs were user-defined. For RhoA activity experiments, cells in different
661 fields of view were selected by a user, cells were then segmented with a custom pixel-
662 classifier based on a pre-trained VGG16 convolutional neural network (Hinderling et al.,
663 2024), which was trained on a field of view of the experimental data. ROIs for stimulation
664 masks were then automatically defined at the top and bottom of the cell for consecutive
665 illumination with different light pulse regimes using our method for automated optogenetic
666 targeting (Hinderling et al., 2025). Fields of views were imaged one after the other on
667 multiple cells. For data extraction the stimulation mask was expanded by gaussian
668 smoothing and then thresholded to cover a wider region, reducing artifacts caused by
669 membrane dynamics. Image intensities were calculated for the overlap of this mask with
670 the segmented cells and the full segmented cells respectively.

671

672 **Immuno-histochemistry**

673 One hour after seeding, cells were fixed for 10 minutes with 0.2% paraformaldehyde. A
674 0.1% Triton X solution was used for permeabilization, after which cells were incubated
675 overnight at 4C with the blocking buffer, containing 5% Bovine-Serum-Albumin and 0.05%
676 Tween20 in PBS. After each step of the following protocol cells were washed three times
677 with Phosphate-Buffered-Saline (PBS). Cells were incubated overnight with the primary

antibody (1:250 dilution for paxillin (Abcam ab32084), 1:50 for pMLC (Cell Signaling Antibody #3671). Secondary antibody incubation (1:1000) lasted one hour. Phalloidin incubation (1:200 Phalloidin-Atto647N) was performed for 20 minutes and DAPI incubation for 10 hours. Cells were imaged immediately after the last step.

Image analysis

Lamella size, focal adhesion areas (Figure 1) and RhoA activity ratio measurements (Figure 3) were computed with CellProfiler in conjunction with a pixel classifier trained with Ilastik (Berg et al., 2019). Spreading dynamics (Figure 2D) were manually analyzed. FRET ratio images were computed and analyzed with custom python scripts. DLC1 and paxillin dynamics (Figure S4D) were calculated with manually drawn ROIs in Fiji (Schindelin et al., 2012).

ODE model and data fitting

For data fitting and parameters optimisation, we used the Julia programming language and tools made available by the Scientific Machine Learning (SciML) organization as framework. The packages ModelingToolkit.jl (Ma et al., 2022) and DifferentialEquations.jl (Rackauckas and Nie, 2017) allowed to symbolically define and solve the ODE system. The ODE solver algorithm was specified as Rodas4P method. In addition, we used the automatic switching algorithm AutoVern9 (Verner, 2010) for stiffness detection. For the parameter optimization, we defined the problem with the package Optimization.jl (Dixit and Rackauckas, 2023). The gradient-based method L-BFGS (Wright et al., 2006) was used as optimization solver from the packages Optim.jl (K Mogensen and N Riseth, 2018). Additionally, the packages SciMLSensitivity.jl (Rackauckas et al., 2021) and ForwardDiff.jl (Revels et al., 2016) were required for an efficient and automatic computation of the gradient with forward propagation. Initial conditions were set to zero for all model species ($\mathrm{Rho^*}_0$,$\mathrm{GAP^*}_0$ $\mathrm{GEF^*}_0$). Total protein concentrations were assumed to be conserved between active and inactive forms. Given the low concentrations at which the system operates, and the relatively small fraction of protein that becomes activated, changes in the inactive pool were considered negligible. As a result, the inactive species were assumed to remain constant throughout the simulation.

To estimate the activation and deactivation rates of optoLARG, we fitted a simple linear model to experimental measurements of membrane recruitment. In the case of RhoA signaling model, Michaelis-Menten kinetics were used to model the interactions between active species, apart from GAP inactivation which was treated as a first-order (linear) deactivation process.

In the *DLC1* KO condition, the Michaelis-Menten constant (Km) of RhoA-dependent GAP activation consistently converged toward zero during optimization, indicating a loss of negative feedback regulation. To reflect this and simplify the model, we explicitly set this parameter to zero, resulting in a reduced model in which GAP activity is independent of RhoA levels. This simplified configuration still produced a strong fit to the experimental data, supporting the hypothesis that the feedback loop regulating GAP activity is disrupted in the KO condition.

We also assessed whether model parameters are uniquely recoverable in principle from the observation scheme using StructuralIdentifiability.jl (Dong et al., 2023). For both the WT and *DLC1* KO ODE model presentations, we ran the package's known-initial-conditions workflow with our initial states treated as known and fixed (here set to 0) and default probabilistic settings (probability threshold 0.99). The analysis returns whether each parameter (and selected parameter functions) is globally identifiable given the model equations and measured outputs, i.e., independent of data noise or sampling.

The following table summarizes the results of the structural identifiability analysis:

Parameter	**Membrane (WT)**	**Membrane (*DLC1* KO)**	**FAs (WT)**	**FAs (*DLC1* KO)**	**Comment**
$V_{\mathrm{ON}}^{\mathrm{GAP}}$	25.2255	21.51569	33.706	15.6152	*alias* $k_{\mathrm{ON}}^{\mathrm{GAP}}$ *for the DLC1 KO adapted model*
Km^{GAP}	0.093982	→ 0	0.205939	→ 0	*consistent across fits*
$k_{\mathrm{OFF}}^{\mathrm{GAP}}$	66.0697	68.84138	99.9969	59.1818	*varied with upper parameter bound*
$V_{\mathrm{ON}}^{\mathrm{Rho}}$	0.0061944	0.00997069	0.00457155	0.00759578	*consistent across fits*
$Km_{\mathrm{ON}}^{\mathrm{Rho}}$	0.0118618	0.031674	0.0108763	0.0382543	*consistent across fits*
$V_{\mathrm{OFF}}^{\mathrm{Rho}}$	25.2258	21.5156	26.7483	15.6151	*varied with upper parameter bound*
$Km_{\mathrm{OFF}}^{\mathrm{Rho}}$	60.6878	94.83013	76.8346	98.2568	*varied with upper parameter bound*

Code availability

The code used to obtain the presented results can be found in the GitHub repository *RhoAModelling* (https://github.com/girochat/RhoAModelling/tree/main) as Pluto and Jupyter notebooks. It contains the model and data fitting of RhoA dynamics at FAs and membrane as well as the parameter estimation of optoLARG dynamics. The Pluto.jl package offers a Julia programming environment analog to Jupyter notebook. For reproducibility, the repository describes how to set a similar coding environment and references all packages that were used.

Acknowledgements

This work was supported by the Swiss National Science Foundation IZSAZ3_173462 Argentinian-Swiss Joint Research Programme and by the Sinergia CRSII5_183550 grants to Olivier Pertz. We are grateful to the Microscopy Imaging Center of the University of Bern for support (https://www.mic.unibe.ch). We thank Kazuhiro Aoki (NIBB, Japan) for providing the pPBbsr2 vector, David L. Hacker (EPFL, Switzerland), for the pPuro-PB and pHygro-PB plasmids, Judith Trüb (UniBE, Switzerland) for the cloning of pB3.0-BLAST, Monilola A. Olayioye (University of Stuttgart, Germany) for the eGFP DLC1 plasmid, Dean E. Natwick and Sean R. Collins (University of California Davis) for sharing the Stargazin-iLID constructs. We are grateful to Miguel Vicente-Manzanares, Bernhard Wehrle-Haller and Daniel Riveline for constructive comments on the manuscript

Author contributions

O.P. supervised the research. O.P., M.H. and L.H. wrote the paper. M.H. designed and performed experiments. L.H. designed and performed optogenetic experiments. G.R. developed and implemented the models. J.v.U. built the optoLARG/rGBD circuit. L.D. developed the optoLARG-mScarlet3 construct. M.D. designed data analysis tools.

Additional Information

The authors declare no competing interests.

757 # Figure legends.

758 **Figure 1. Cytoskeletal structures in WT and DLC1 deficient cells.**

759 **A,B.** Representative immunofluorescence images of paxillin and F-actin (phalloidin) (**A**),
760 and pMLC and F-actin (phalloidin) (**B**) immunostains are shown in inverted black and white
761 (ibw) contrast as well as color composites (DAPI signal also included). Scale bar = 10µm.

762 **C.** Compared to WT cells (n=243) lamella size is significantly increased in *DLC1* KD cells
763 (n=290, p-adjusted < 0.001) and *DLC1* KO cells (n=242, p-adjusted < 0.001), while *DLC1*
764 rescue cells (n=57) show significantly lower lamella sizes than both, WT (p-adjusted =
765 0.0098), as well as KO cells (p-adjusted < 0.001).

766 **D.** *DLC1* KD cells (n=290) display a significant increase in the total area of focal adhesions
767 per cell (p-adjusted <0.001) compared to WT cells (n=243), while *DLC1* KO cells (n=242)
768 do not show a significant difference (p-adjusted = 0.09). Rescue cells show a significant
769 decrease in the total area of focal adhesions (p-adjusted < 0.001). ANOVA plus Tukey's
770 honestly significant difference test.

771

772 **Figure 2. F-actin dynamics and cell morphodynamics in WT and *DLC1* KO**
773 **cells.**

774 All time series are representative ibw contrast images of WT and *DLC1* KO cells expressing
775 Lifeact-mCherry. Dotted lines mark the area used for the kymographs shown in the right
776 panels.

777 **A.** Cells were imaged for 10 minutes in 10 second intervals during spreading immediately
778 after replating. Dotted red lines display differences in lamella size in WT and *DLC1* KO
779 cells. Time

780 **B.** One hour after reseeding, when cells are still isotropically spreading, *DLC1* KO cells
781 display increased lamellipodia size and more prominent edge protrusion retraction cycles.
782 High magnification insets are shown for time point 10 minutes and show the robust increase
783 of contractility in *DLC1* KO cells.

784 **C.** Cells were imaged for 10 hours with 15 minutes intervals starting from spreading. WT
785 cells break symmetry and display episodes of polarized motility. KO cells are much less
786 dynamic and reach a contractile phenotype much faster, without being able to polarize.

787 **D.** Box plot showing at which time point cells exhibited the elongated phenotype described
788 in (**C**). *DLC1* KO cells (n=42) exhibited this phenotype a mean of 90 minutes earlier than
789 WT cells (n=22) p-adjusted = 0.002, Student's t-test. 17 additional WT cells failed to
790 develop that phenotype entirely.

791 Scale bars = 20 μm for all images.

792

793 **Figure 3. RhoA activation dynamics in WT and *DLC1* KO cells**

794 Cells are stably expressing Lifeact-mCherry, and the RhoA2G FRET sensor. RhoA
795 localization images show RhoA2G localization that is identical to RhoA. RhoA activity
796 images display the computed FRET ratio. Images are color-coded according to the
797 normalized scales shown below the panels.

798 **A**. Representative images of WT and *DLC1* KO cells during spreading. Kymographs for the
799 violet lines are shown in the right panels. Note the RhoA activity band maintains constant
800 width during spreading at the periphery in WT cells. Note increased global RhoA activity in
801 *DLC1* KO cells, with maintenance of a similar RhoA band pattern at the cell edge.

802 **B.** Box plots of FRET ratio averaged over the whole cell (right panel) or a ROI placed at
803 the cell edge (left panel). This shows that during spreading *DLC1* KO cells (n = 149) have
804 an increased total RhoA activity compared to WT cells (n = 114, p = 0.005). In addition, the
805 FRET ratio at just the cell edge is increased as well (p=0.011).

806 **C.** Representative images of WT cells and DLC1 KO cells that have transitioned in a
807 contractile state 12 hours after plating. No difference in RhoA activity pattern can be
808 observed between WT and *DLC1* KO cells, although the latter still display slightly higher
809 global RhoA activity levels.

810 **D.** Box plots of FRET ratio averaged over the whole cell (right panel) or a ROI placed at
811 the cell edge (left panel). This shows that contractile *DLC1* KO cells (n=103) have an
812 increased total RhoA activity (p < 0.001) and edge FRET ratio (p < 0.001) compared to WT
813 cells (n = 82) compared to WT cells (n = 82). Students t-test.

814 (A,B) Scale bars = 20 μm.

815

816 **Figure 4. An optogenetic actuator- Rho biosensor circuit to probe Rho**
817 **GTPase flux**

818 **A.** Schematics of the optogenetic actuator - Rho biosensor to measure Rho GTPase flux.
819 OptoLarg is based on an iLID system which does not interact with Ssb-LARG in the dark
820 state. The iLID module is anchored to the PM by a Stargazin anchor that displays slow
821 diffusion, allowing better focussing of optogenetic activation. Upon light exposure ssb-
822 LARG is locally recruited to the plasma membrane, activating Rho. Rho activity is
823 measured by a rGBD effector binding domain.

824 **B.** Time-series of REF52 cells locally stimulated with light first in a ROI at the cell top with
825 a high stimulation frequency, and then with a ROI at the cell bottom with a low stimulation
826 frequency. Light pulses have the same intensity. Thick and thin blue thunder symbols
827 represent high and low optogenetic stimulation. Red dotted line is used for the kymograph
828 shown in (C).

829 **C.** Kymographs of cells in (B). Light pulse stimulation regimes of top and bottom ROIs are
830 shown in the upper box. Blue dotted boxes indicate the region and length of the stimulation.

831 Note how intense optogenetic stimulation in the top ROI leads to Rho activity, assembly of
832 contractile F-actin structures, and robust edge retraction. Upon removal of the light input,
833 the Rho activity and F-actin resume, and edge protrusion occurs again. Lower optogenetic
834 stimulation in the bottom ROI leads to much lower Rho activity and F-actin structures, as
835 well as lower edge retraction.

836 (**B**,**C**) Scale bars = 10 µm

837

838 **Figure 5. Rho GTPase activation kinetics in WT versus DLC1 KO cells**

839 **A.** Computer vision pipeline and experiment: 1) a cell is segmented using the rGBD-dTomato
840 channel. 2) FAs and non-FAs are detected using the paxillin channel (see Material and
841 Methods). ROIs on FAs (blue dots, shown in the bottom left panel) and ROIs on non-FA
842 regions in between (orange dots, shown in the upper left panel) are selected for stimulation.
843 3) Image of the stimulation pattern (green channel) shows that the calibrated DMD can
844 stimulate the regions with high spatial precision (image is overexposed to show the
845 diffraction pattern of the mirrors).

846 **B.** The DMD is used to stimulate ROIs (FAs or non-FAs) with a pulse of blue light (blue line).
847 rGBD signal fluctuations are then measured in the ROIs.

848 **C.** Distribution of paxillin-miRFP intensities in the FA and non-FA ROIs normalized to the
849 mean paxillin-miRFP intensity of the whole cell shows that our segmentation pipeline
850 accurately identifies FA and non-FA ROIs.

851 **D.** Paxillin-miRFP fluorescene of stimulated ROIs, normalized to the mean paxillin intensity
852 of the whole cell. Median and 99% CI are shown. Intensity of paxillin does not change upon
853 stimulation, indicating that the stimulation is too weak to trigger reinforcement of focal
854 adhesions (compare to Figure 7A-D).

855 **E.** Normalized and averaged rGBD fluorescence fluctuations upon ROI optogenetic
856 stimulation. For each stimulated ROIs, the fold change to the baseline (average activity from
857 0-150 seconds before optogenetic stimulation) is calculated. Median and 99% CI are shown.
858 Regions on top of focal adhesions have a larger fold change in rGBD activity than regions

859 between focal adhesions. *DLC1* KO cells have a larger rGBD fold change in the initial time
860 after stimulation (150-200 seconds), but then also fall back down to the baseline quicker.
861 (KO FA: N = 3643, KO non-FA: N = 3643, WT FA: N = 2144, WT non-FA: N = 2144. Mean
862 number of regions per cell: ~16.90, Cells WT = 321, *DLC1* KO = 431. The same cell can
863 appear multiple times in the experiment, but with a relaxation time in between and new
864 stimulation regions).

865 **F.** The different dynamics described in (**E**) can be robustly observed in technical replicates
866 of the experiment. In all replicates the rGBD recruitment is higher in FAs vs non-FAs, and
867 we see the trend of faster accumulation and faster return to baseline of rGBD in *DLC1* KO
868 vs WT cells.

869 **Figure 6. Mathematical Model of RhoA differential activation/deactivation**
870 **dynamics in WT vs. *DLC1* KO cells**
871
872 **A.** Schematics of RhoA activation/deactivation system that correspond to the ODE model
873 of RhoA dynamics. The light pulse increases GEF activation rate, which in turn increases
874 RhoA activation. Active RhoA activates GAP, negatively auto-regulating itself. RhoA
875 deactivation is mediated by active GAPs. Detailed description of modeling approach is
876 provided in the Methods section.

877 **B.** Results after fitting the ODE model to the data for both RhoA dynamics at the membrane
878 (left panel) and at focal adhesions (right panel). WT and *DLC1* KO conditions were fitted
879 separately in each case. The fold-change to the baseline of averaged and normalized rGBD
880 intensity was taken as datapoint for each acquisition frame.

881 **C.** Illustration of the dynamics of the other model species that are active GEF and active
882 GAP after the light pulse trigger. The left panel shows the dynamics at the membrane, right
883 panel at focal adhesions.

884 **Figure 7. Optogenetic control of force-dependent DLC1 interactions with FAs**

885 **A.** Color-coded fluorescence micrographs of REF52 fibroblast expressing miRFP-paxillin
886 (left) and mCherry-DLC1 (right) and the optoLARG construct (not shown). The black boxes
887 indicate the area used for close up images in (B). The white boxes indicate the ROI for
888 optogenetic illumination. Selected FAs denoted by the pink and green arrowheads. The
889 black dotted lines were used for the kymograph in B.

890 **B.** Kymographs showing two selected FAs, the grey box indicates the time at which
891 optogenetic stimulation has been applied. Optogenetic stimulation is applied on select
892 ROIs placed over FAs with 50 ms light pulses per frame (every 15 seconds) for a duration
893 of 7.5 minutes.

894 **C.** Closeups time series of paxillin and DLC1 signals at a single FA denoted by the
895 respective arrowheads. Scale bars = 10 µm.

896 **D.** Quantification of mcherry-DLC1 and miRFP-paxillin fluorescence signals during
897 optoLARG mediated control of FA reinforcement and relaxation. Normalized miRFP-
898 paxilllin and mCherry-DLC1 from 2 FAs shown in panels A-C.

899 **E.** Model of Rho GTPase activity modulation by DLC1 at FAs and at the plasma membrane
900 relevant to Figure 5. Left and right panels show schematics of Rho activation dynamics in
901 response to optoLARG optogenetic input at FAs (left panel) and plasma membrane (right
902 panels). Top and bottom panel show schematics for Rho activation dynamics in response
903 to optoLARG optogenetic input in control (top) and DLC1 KO (bottom) panels.

904 **F.** Model of force dependent regulation of DLC1 at FAs relevant to this and Figure S4. Left
905 panel, in absence of acute mechanical input, DLC1 increases with FA assembly and
906 decreases with FA disassembly. Central panel, upon acute local increase of mechanical
907 stress in response to application of an optoLARG optogenetic input, DLC1 unbinds from
908 FA in a reinforcement regime, and rebinds FA in a relaxing regime when the optoLARG
909 input is removed. Right panel, upon acute local increase of mechanical stress in response
910 to application of an optoLARG optogenetic input some FAs rupture after DLC1 dissociation
911 and FA rupture.

912 Supplementary Figure legends

913 **Figure S1: Cell motility properties in WT versus DLC1 KO cells**

914 **A.** Example fields of view of tracked WT and DLC1 KO cells. 20000 REF fibroblasts
915 expressing a histone H2B-miRFP marker were seeded in a 24 well-plate well coated with
916 fibronectin and stimulated with 20 ng/ml PDGF, imaged for 12 hours at 15 minutes interval.
917 Tracking was performed using stardist 37 on the H2B image). DLC1 KO cells display a
918 large subpopulation of cells that remain extremely stationary.

919 **B.** Mean Square displacements (MSDs) for different time intervals, WT move more than
920 *DLC1* KO cells for all possible lag times. Plot shows directionality (exponential bit between
921 0.25 and 1.5 hours). For times longer than 2 hours the curve is flat indicating that migration
922 has characteristics of random walk at these timescales. Thick lines: mean, thin lines:
923 standard deviation. Dotted grey line shows delta t chosen for figure C.

924 **C.** Distribution of velocities calculated as µm/hour from Root-MSD. We again observe the
925 bimodal distribution in the *DLC1* KO cell with a big subgroup of the cells move extremely
926 slowly (5 µm/hour). Thick lines are mean and extrema. Two sided t-test: (statistic=25.1, p-
927 value=1.6e-131)

928

929 **Figure S2. Effect of DLC1 overexpression on F-actin cytoskeleton and RhoA**
930 **activity**

931 **A.** Effect of DLC1 overexpression of F-actin. REF52 cells stably expressing Lifeact-
932 mCherry were transfected with mCherry-DLC1 or mCherry plasmids, allowed to spread for
933 12 hours on fibronectin-coated coverslips and imaged. Images are shown in ibw contrast.
934 Large mCherry-DLC1 pool in the cytosol levels documents its overexpression. Note how
935 DLC1 overexpression leads to loss of contractile F-actin structures.

936 **B.** Effect of DLC1 overexpression of RhoA. Cells stably transfected with the RhoA2G
937 biosensor were transfected with mCherry-paxillin or mCherry-DLC1. mCherry signals are
938 shown in ibw contrast. RhoA2G FRET ratio, and expression levels are color-coded
939 according to the scale. Note how low mCherry-DLC1 expression that remains associated
940 with FA already lowers RhoA activity, while high mCherry-DLC1 expression leads to even
941 lower RhoA activity and aberrant cell morphology.

942

943 **Figure S3: Quantification of optoLARG recruitment dynamics to subcellular**
944 **locations.**

945 **A.** optoLARG recruitment over time shows similar dynamics to FA ROIs (N=190) and non-
946 FA ROIs (N=184) regions (background subtracted, divided by mean optoLARG expression
947 in the cell and normalized to baseline of first 10 frames / 100 s). Mean of all ROIs and 99%
948 CI are shown.

949 **B.** Comparing optoLARG recruitment at peak response (t = 200 s), averaging all FA/non-
950 FA ROIs within same cell. Wilcoxon paired test shows no significant difference between
951 the two conditions (cells N = 39, p = 0.419, mean FA: 1.1450 ± 0.23, mean NON-FA: 1.1884
952 ± 0.22).

953 **C.** Characterization of optoLARG recruitment dynamics. As FA and non-FA regions shows
954 similar dynamics, here we average all ROIs. To quantify the kinetics of recruitment and
955 dissociation, we fit the mean normalized and drift-corrected time series with piecewise
956 exponential models. The rising phase during stimulation (150-200 s) was well described by
957 an inverse exponential function, with an amplitude of 0.166 and a half-life of 7.9 seconds
958 ($R^2 = 0.991$, RSS = $1.88*10^{-4}$). The decay phase (200-300 s) was well described by a single
959 exponential decay with a half-life of 10.8 seconds and a slightly lower amplitude of 0.164
960 ($R^2 = 0.989$, RSS = $3.24*10^{-4}$).

961

962 **Figure S4. DLC1 dynamics at FAs in unperturbed cells**

963 Panels **A-C** document FAs in an assembly state. This shows that the DLC1 signal
964 augments concomitantly with paxillin signal during FA assembly.

965 Panels **D-F** document FAs in a disassembly state. This shows that the DLC1 signal
966 decreases concomitantly with paxillin signal during FA disassembly.

967 **A,D.** Color-coded fluorescence micrographs of REF52 fibroblast expressing miRFP-paxillin
968 (top) and mCherry-DLC1 (bottom). The white boxes indicate the area used for close up
969 images in (B,E).

970 **B,E.** Closeups of the ROIs (left panel) and kymographs (right panel) of selected FAs
971 denoted by the red arrowheads. White dotted lines were used for the kymograph. In the
972 kymograph, the grey box indicates the time at which optogenetic stimulation has been
973 applied.

974 **C,F.** Closeups time series of paxillin and DLC1 signals at a single FA denoted by the
975 respective red arrowheads.

976 Scale bars = 10 μm.

977

978 **Figure S5. DLC1 dynamics in an optoLARG stimulated FA that undergoes**
979 **reinforcement followed by disassembly, as well as FA behavior in absence**
980 **of optoLARG stimulus**

981 Panels **A-C** document FAs that when subjected to a nearby pulse of optogenetic Rho-
982 mediated contractility display a behavior of FA reinforcement followed by disassembly.
983 Optogenetic stimulation is applied on select ROIs placed over FAs with 50 ms light pulses
984 per frame (every 15 seconds) for a duration of 8 minutes.

985 Panels **D-F** document the dynamics of DLC1 in a ROI not stimulated with light in the same
986 cell as in shown in Figure 6A-C.

987 **A.** Color-coded fluorescence micrographs of REF52 fibroblast expressing miRFP-paxillin
988 (top) and mCherry-DLC1 (bottom) and the optoLARG construct (not shown). The black
989 boxes indicate the area used for close up images in (B). The white boxes indicate the ROI
990 for optogenetic illumination.

991 **B.** Closeups of the ROIs (left panel) and kymographs (right panel) of selected FAs denoted
992 by the arrowheads. The pink and green arrowheads indicate the FAs of interest in (B). The
993 black arrowhead indicates the FA of interest in (C). The black dotted lines were used for
994 the kymograph. In the kymograph, the grey box indicates the time at which optogenetic
995 stimulation has been applied.

996 **C.** Closeups time series of paxillin and DLC1 signals at a single FA denoted by the
997 respective arrowheads. Scale bars = 10 µm.

998 **D.** Color-coded fluorescence micrographs of REF52 fibroblast expressing miRFP-paxillin
999 (top) and mCherry-DLC1 (bottom) and the optoLARG construct (not shown). The black
1000 boxes indicate the area used for close up images in (B,E). The white boxes indicate the
1001 ROI for optogenetic illumination.

1002 **E.** Closeups of the ROIs (left panel) and kymographs (right panel) of selected FAs denoted
1003 by the arrowheads. The pink and green arrowheads indicate the FAs of interest in (B). The
1004 black arrowhead indicates the FA of interest in (D). The black dotted lines were used for
1005 the kymograph. In the kymograph, the grey box indicates the time at which optogenetic
1006 stimulation has been applied.

1007 **F.** Closeups time series of paxillin and DLC1 signals at a single FA denoted by the
1008 respective arrowheads.

1009

1010 Supplementary Movie legends

1011 **Movie S1: F-actin dynamics of WT and DLC1 KO REF52 cells during late**
1012 **spreading (relevant to Figure 2B).**

1013 Representative ibw contrast movie of WT and *DLC1* KO cells expressing Lifeact-mCherry
1014 during late spreading. Time: Minutes:seconds. Scale bar = 20 mm.

1015

1016 **Movie S2: F-actin dynamics and edge dynamics of WT and DLC1 KO REF52**
1017 **cells during acquisition of a polarized cell migration phenotype over a period**
1018 **of 15 hours (relevant to Figure 2C).**

1019 Representative ibw contrast movie of WT and *DLC1* KO cells expressing Lifeact-mCherry
1020 for 15. Edge dynamics were color-coded with respect to time. Time: Minutes:seconds.
1021 Scale bar = 20 mm.

1022

1023 **Movie S3: F-actin and RhoA activity dynamics WT and DLC1 KO REF52 cells**
1024 **during late spreading (relevant to Figure 3A).**

1025 Representative movie of WT and *DLC1* KO cells expressing Lifeact-mCherry and the
1026 RhoA2G FRET biosensor during late spreading.

1027 Left panels: F-actin channel in ibw contrast. Right panels: RhoA activity emission ratio color
1028 coded according to color scale.

1029 Time: Minutes:seconds. Scale bar = 20 mm.

1030

1031 **Movie S4: Characterisation of the optoLARG/rGBD genetic circuit (relati to**
1032 **Figure 5)**

1033 REF52 cells stably expressing the optoLARG/rGBD circuit as well as Lifeact-miRFP are
1034 locally stimulated with blue light of identical intensity, first in a ROI at the cell top with a high
1035 stimulation frequency, and then with a ROI at the cell bottom with a lower stimulation
1036 frequency. The stimulation frequencies are indicated by the appearance/disappearance
1037 frequency of the ROIs.

1038 Left panel: rGBD signal, Right panel: F-actin lifeact-miRFP. Note the more robust edge
1039 contraction, as well as increased RhoA activity in response to high versus low light
1040 frequency stimulation.

1041 Time: Minutes:seconds. Scale bar = 10 mm.

1042

1043 **Movie S5: DLC1 dynamics at FAs during an optoLARG-induced contractility**
1044 **pulse (relevant to Figure 6A-C, cell denoted by pink arrow)**

1045 REF52 KO cells rescued with mCherry-DLC1 and expressing miRFP-paxillin, and the
1046 optoLARG/rGBD circuit were imaged before, during and after a transient optogenetic
1047 stimulation in the whole field of view shown in the movie.

1048 Time: Minutes:seconds. Scale bar = 5 mm.

References

Basant A, Glotzer M. 2018. Spatiotemporal Regulation of RhoA during Cytokinesis. *Curr Biol* **28**:R570–R580. doi:10.1016/j.cub.2018.03.045

Bement WM, Goryachev AB, Miller AL, Von Dassow G. 2024. Patterning of the cell cortex by Rho GTPases. *Nat Rev Mol Cell Biol* **25**:290–308. doi:10.1038/s41580-023-00682-z

Bement WM, Leda M, Moe AM, Kita AM, Larson ME, Golding AE, Pfeuti C, Su K-C, Miller AL, Goryachev AB, von Dassow G. 2015. Activator-inhibitor coupling between Rho signalling and actin assembly makes the cell cortex an excitable medium. *Nat Cell Biol* **17**:1471–1483.

Bement WM, von Dassow G. 2014. Single cell pattern formation and transient cytoskeletal arrays. *Curr Opin Cell Biol* **26**:51–59.

Berg S, Kutra D, Kroeger T, Straehle CN, Kausler BX, Haubold C, Schiegg M, Ales J, Beier T, Rudy M, Eren K, Cervantes JI, Xu B, Beuttenmueller F, Wolny A, Zhang C, Koethe U, Hamprecht FA, Kreshuk A. 2019. ilastik: interactive machine learning for (bio) image analysis. *Nat Methods* **16**:1–7.

Blum Y, Mikelson J, Dobrzyński M, Ryu H, Jacques M-A, Jeon NL, Khammash M, Pertz O. 2019. Temporal perturbation of ERK dynamics reveals network architecture of FGF2/MAPK signaling. *Mol Syst Biol* **15**:e8947. doi:10.15252/msb.20198947

De Seze J, Gatin J, Coppey M. 2023. RhoA regulation in space and time. *FEBS Lett* **597**:836–849. doi:10.1002/1873-3468.14578

DerMardirossian C, Rocklin G, Seo J-Y, Bokoch GM. 2006. Phosphorylation of RhoGDI by Src regulates Rho GTPase binding and cytosol-membrane cycling. *Mol Biol Cell* **17**:4760–4768. doi:10.1091/mbc.e06-06-0533

Dessauges C, Mikelson J, Dobrzyński M, Jacques M, Frismantiene A, Gagliardi PA, Khammash M, Pertz O. 2022. Optogenetic actuator – ERK biosensor circuits identify MAPK network nodes that shape ERK dynamics. *Mol Syst Biol* **18**. doi:10.15252/msb.202110670

Dixit VK, Rackauckas C. 2023. Optimization.jl: A Unified Optimization Package. doi:10.5281/ZENODO.7738525

Dong R, Goodbrake C, Harrington HA, Pogudin G. 2023. Differential Elimination for Dynamical Models via Projections with Applications to Structural Identifiability. *SIAM J Appl Algebra Geom* **7**:194–235. doi:10.1137/22M1469067

Edelstein AD, Tsuchida MA, Amodaj N, Pinkard H, Vale RD, Stuurman N. 2014. Advanced methods of microscope control using μManager software. *J Biol Methods* **1**. doi:10.14440/jbm.2014.36

Erlmann P, Schmid S, Horenkamp FA, Geyer M, Pomorski TG, Olayioye MA. 2009. DLC1 activation requires lipid interaction through a polybasic region preceding the RhoGAP domain. *Mol Biol Cell* **20**:4400–4411. doi:10.1091/mbc.e09-03-0247

Etienne-Manneville S, Hall A. 2002. Rho GTPases in cell biology. *Nature* **420**:629–635.

Fritz RD, Letzelter M, Reimann A, Martin K, Fusco L, Ritsma L, Ponsioen B, Fluri E, Schulte-Merker S, van Rheenen J, Pertz O. 2013. A versatile toolkit to produce sensitive FRET biosensors to visualize signaling in time and space. *Sci Signal* **6**:rs12. doi:10.1126/scisignal.2004135

Fritz RD, Pertz O. 2016a. The dynamics of spatio-temporal Rho GTPase signaling: formation of signaling patterns. *F1000Research* **5**. doi:10.12688/f1000research.7370.1

Fritz RD, Pertz O. 2016b. The dynamics of spatio-temporal Rho GTPase signaling: formation of signaling patterns. *F1000Research* **5**:F1000 Faculty Rev-749. doi:10.12688/f1000research.7370.1

Fusco L, Lefort R, Smith K, Benmansour F, Gonzalez G, Barillari C, Rinn B, Fleuret F, Fua P, Pertz O. 2016. Computer vision profiling of neurite outgrowth dynamics reveals spatiotemporal modularity of Rho GTPase signaling. *J Cell Biol* **212**:91–111. doi:10.1083/jcb.201506018

Gingras AR, Bate N, Goult BT, Hazelwood L, Canestrelli I, Grossmann JG, Liu H, Putz NSM, Roberts GCK, Volkmann N, Hanein D, Barsukov IL, Critchley DR. 2008. The structure of the C-terminal actin-binding domain of talin. *EMBO J* **27**:458–469. doi:10.1038/sj.emboj.7601965

Goult BT, Brown NH, Schwartz MA. 2021. Talin in mechanotransduction and mechanomemory at a glance. *J Cell Sci* **134**:jcs258749. doi:10.1242/jcs.258749

Graessl M, Koch J, Calderon A, Kamps D, Banerjee S, Mazel T, Schulze N, Jungkurth JK, Patwardhan R, Solouk D, Hampe N, Hoffmann B, Dehmelt L, Nalbant P. 2017. An excitable Rho GTPase signaling network generates dynamic subcellular contraction patterns. *J Cell Biol* **17**:jcb.201706052-15.

Guntas G, Hallett RA, Zimmerman SP, Williams T, Yumerefendi H, Bear JE, Kuhlman B. 2015. Engineering an improved light-induced dimer (iLID) for controlling the localization and activity of signaling proteins. *Proc Natl Acad Sci U S A* **112**:112–117.

Gutenkunst RN, Waterfall JJ, Casey FP, Brown KS, Myers CR, Sethna JP. 2007. Universally Sloppy Parameter Sensitivities in Systems Biology Models. *PLoS Comput Biol* **3**:e189. doi:10.1371/journal.pcbi.0030189

Haining AWM, Rahikainen R, Cortes E, Lachowski D, Rice A, von Essen M, Hytönen VP, del Río Hernández A. 2018. Mechanotransduction in talin through the interaction of the R8 domain with DLC1. *PLOS Biol* **16**:e2005599-20.

Hallett RA, Zimmerman SP, Yumerefendi H, Bear JE, Kuhlman B. 2016. Correlating in Vitro and in Vivo Activities of Light-Inducible Dimers: A Cellular Optogenetics Guide. *ACS Synth Biol* **5**:53–64. doi:10.1021/acssynbio.5b00119

Hinderling L, Landolt AE, Grädel B, Dubied L, Zahni C, Kwasny M, Frismantiene A, Lambert T, Dobrzyński M, Pertz O. 2025. Real-time feedback control microscopy for automation of optogenetic targeting. doi:10.1101/2025.08.17.670729

Hinderling L, Witz G, Schwob R, Stojiljkovic A, Dobrzynski M, Vladymyrov M, Frei J, Graedel B, Frismantiene A, Pertz O. 2024. Convpaint - Universal framework for interactive pixel classification using pretrained neural networks. doi:10.1101/2024.09.12.610926

Hu J, Gong X, Strömblad S. 2022. Local temporal Rac1-GTP nadirs and peaks restrict cell protrusions and retractions. *Sci Adv* **8**:eabl3667. doi:10.1126/sciadv.abl3667

Isogai T, Danuser G. 2018. Discovery of functional interactions among actin regulators by analysis of image fluctuations in an unperturbed motile cell system. *Philos Trans R Soc B Biol Sci* **373**:20170110. doi:10.1098/rstb.2017.0110

Itoh RE, Kurokawa K, Ohba Y, Yoshizaki H, Mochizuki N, Matsuda M. 2002. Activation of Rac and Cdc42 Video Imaged by Fluorescent Resonance Energy Transfer-Based Single-Molecule Probes in the Membrane of Living Cells. *Mol Cell Biol* **22**:6582–6591. doi:10.1128/MCB.22.18.6582-6591.2002

K Mogensen P, N Riseth A. 2018. Optim: A mathematical optimization package for Julia. *J Open Source Softw* **3**:615. doi:10.21105/joss.00615

Kaushik S, Ravi A, Hameed FM, Low BC. 2014. Concerted modulation of paxillin dynamics at focal adhesions by deleted in liver cancer-1 and focal adhesion kinase during early cell spreading: DLC1 Regulates Paxillin Dynamics at Focal Adhesions via FAK. *Cytoskeleton* **71**:677–694. doi:10.1002/cm.21201

Kraynov VS, Chamberlain C, Bokoch GM, Schwartz MA, Slabaugh S, Hahn KM. 2000. Localized Rac activation dynamics visualized in living cells. *Science* **290**:333–337.

Krendel M, Zenke FT, Bokoch GM. 2002. Nucleotide exchange factor GEF-H1 mediates cross-talk between microtubules and the actin cytoskeleton. *Nat Cell Biol* **4**:294–301. doi:10.1038/ncb773

Lam NN, Docherty PD, Murray R. 2022. Practical identifiability of parametrised models: A review of benefits and limitations of various approaches. *Math Comput Simul* **199**:202–216. doi:10.1016/j.matcom.2022.03.020

Li G, Du X, Vass WC, Papageorge AG, Lowy DR, Qian X. 2011. Full activity of the deleted in liver cancer 1 (DLC1) tumor suppressor depends on an LD-like motif that binds talin and focal adhesion kinase (FAK). *Proc Natl Acad Sci* **108**:17129–17134. doi:10.1073/pnas.1112122108

Ma Y, Gowda S, Anantharaman R, Laughman C, Shah V, Rackauckas C. 2022. ModelingToolkit: A Composable Graph Transformation System For Equation-Based Modeling. doi:10.48550/arXiv.2103.05244

Machacek M, Hodgson L, Welch C, Elliott H, Pertz O, Nalbant P, Abell A, Johnson GL, Hahn KM, Danuser G. 2009. Coordination of Rho GTPase activities during cell protrusion. *Nature* **461**:99–103. doi:10.1038/nature08242

Mahlandt EK, Arts JJG, van der Meer WJ, van der Linden FH, Tol S, van Buul JD, Gadella TWJ, Goedhart J. 2021. Visualizing endogenous Rho activity with an improved localization-based, genetically encoded biosensor. *J Cell Sci* **134**:jcs258823. doi:10.1242/jcs.258823

Martin K, Reimann A, Fritz RD, Ryu H, Jeon NL, Pertz O. 2016. Spatio-temporal co-ordination of RhoA, Rac1 and Cdc42 activation during prototypical edge protrusion and retraction dynamics. *Sci Rep* **6**:21901. doi:10.1038/srep21901

Martin K, Vilela M, Jeon NL, Danuser G, Pertz O. 2014. A growth factor-induced, spatially organizing cytoskeletal module enables rapid and persistent fibroblast migration. *Dev Cell* **30**:701–716. doi:10.1016/j.devcel.2014.07.022

Matasci M, Baldi L, Hacker DL, Wurm FM. 2011. The PiggyBac transposon enhances the frequency of CHO stable cell line generation and yields recombinant lines with superior productivity and stability. *Biotechnol Bioeng* **108**:2141–2150. doi:10.1002/bit.23167

Miller AL, Bement WM. 2009. Regulation of cytokinesis by Rho GTPase flux. *Nat Cell Biol* **11**:71–77. doi:10.1038/ncb1814

Moon SY, Zheng Y. 2003. Rho GTPase-activating proteins in cell regulation. *Trends Cell Biol* **13**:13–22. doi:10.1016/s0962-8924(02)00004-1

Mosaddeghzadeh N, Ahmadian MR. 2021. The RHO Family GTPases: Mechanisms of Regulation and Signaling. *Cells* **10**:1831. doi:10.3390/cells10071831

Müller PM, Rademacher J, Bagshaw RD, Wortmann C, Barth C, van Unen J, Alp KM, Giudice G, Eccles RL, Heinrich LE, Pascual-Vargas P, Sanchez-Castro M, Brandenburg L, Mbamalu G, Tucholska M, Spatt L, Czajkowski MT, Welke R-W, Zhang S, Nguyen V, Rrustemi T, Trnka P, Freitag K, Larsen B, Popp O, Mertins P, Gingras A-C, Roth FP, Colwill K, Bakal C, Pertz O, Pawson T, Petsalaki E, Rocks O. 2020. Systems analysis of RhoGEF and RhoGAP regulatory proteins reveals spatially organized RAC1 signalling from integrin adhesions. *Nat Cell Biol* **22**:498–511. doi:10.1038/s41556-020-0488-x

Nalbant P, Hodgson L, Kraynov V, Toutchkine A, Hahn KM. 2004. Activation of endogenous Cdc42 visualized in living cells. *Science* **305**:1615–1619.

Natwick DE, Collins SR. 2021. Optimized iLID Membrane Anchors for Local Optogenetic Protein Recruitment. *ACS Synth Biol* **10**:1009–1023. doi:10.1021/acssynbio.0c00511

Oakes PW, Wagner E, Brand CA, Probst D, Linke M, Schwarz US, Glotzer M, Gardel ML. 2017. Optogenetic control of RhoA reveals zyxin-mediated elasticity of stress fibres. *Nat Commun* **8**:15817–12.

Pertz O. 2010. Spatio-temporal Rho GTPase signaling - where are we now? *J Cell Sci* **123**:1841–1850. doi:10.1242/jcs.064345

Pertz O, Hodgson L, Klemke RL, Hahn KM. 2006. Spatiotemporal dynamics of RhoA activity in migrating cells. *Nature* **440**:1069–1072. doi:10.1038/nature04665

Rackauckas C, Ma Y, Martensen J, Warner C, Zubov K, Supekar R, Skinner D, Ramadhan A, Edelman A. 2021. Universal Differential Equations for Scientific Machine Learning. doi:10.48550/arXiv.2001.04385

Rackauckas C, Nie Q. 2017. DifferentialEquations.jl – A Performant and Feature-Rich Ecosystem for Solving Differential Equations in Julia. *J Open Res Softw* **5**:15. doi:10.5334/jors.151

Revels J, Lubin M, Papamarkou T. 2016. Forward-Mode Automatic Differentiation in Julia. doi:10.48550/arXiv.1607.07892

Riedl J, Crevenna AH, Kessenbrock K, Yu JH, Neukirchen D, Bista M, Bradke F, Jenne D, Holak TA, Werb Z, Sixt M, Wedlich-Soldner R. 2008. Lifeact: a versatile marker to visualize F-actin. *Nat Methods* **5**:605–607. doi:10.1038/nmeth.1220

Rochussen AM, Ma CY, Griffiths GM. 2025. Transcriptional adaptation after deletion of *Cdc42* in primary T cells. *J Cell Sci* **138**:jcs263826. doi:10.1242/jcs.263826

Rossman KL, Der CJ, Sondek J. 2005. GEF means go: turning on RHO GTPases with guanine nucleotide-exchange factors. *Nat Rev Mol Cell Biol* **6**:167–180.

Ryu H, Chung M, Dobrzyński M, Fey D, Blum Y, Lee SS, Peter M, Kholodenko BN, Jeon NL, Pertz O. 2015. Frequency modulation of ERK activation dynamics rewires cell fate. *Mol Syst Biol* **11**:838. doi:10.15252/msb.20156458

Schindelin J, Arganda-Carreras I, Frise E, Kaynig V, Longair M, Pietzsch T, Preibisch S, Rueden C, Saalfeld S, Schmid B, Tinevez J-Y, White DJ, Hartenstein V, Eliceiri K, Tomancak P, Cardona A. 2012. Fiji: an open-source platform for biological-image analysis. *Nat Methods* **9**:676–682. doi:10.1038/nmeth.2019

Schmick M, Kraemer A, Bastiaens PIH. 2015. Ras moves to stay in place. *Trends Cell Biol* **25**:190–197.

Tsyganov MA, Kolch W, Kholodenko BN. 2012. The topology design principles that determine the spatiotemporal dynamics of G-protein cascades. *Mol Biosyst* **8**:730–743.

Wu C-F, Lew DJ. 2013. Beyond Symmetry Breaking: Competition and Negative Feedback in GTPase regulation. *Trends Cell Biol* **23**:476–483. doi:10.1016/j.tcb.2013.05.003

Zhao Y, Lykov N, Tzeng C. 2022. Talin-1 interaction network in cellular mechanotransduction (Review). *Int J Mol Med* **49**:1–12. doi:10.3892/ijmm.2022.5116

Figure 1. Cytoskeletal structures in WT and DLC1 deficient cells.

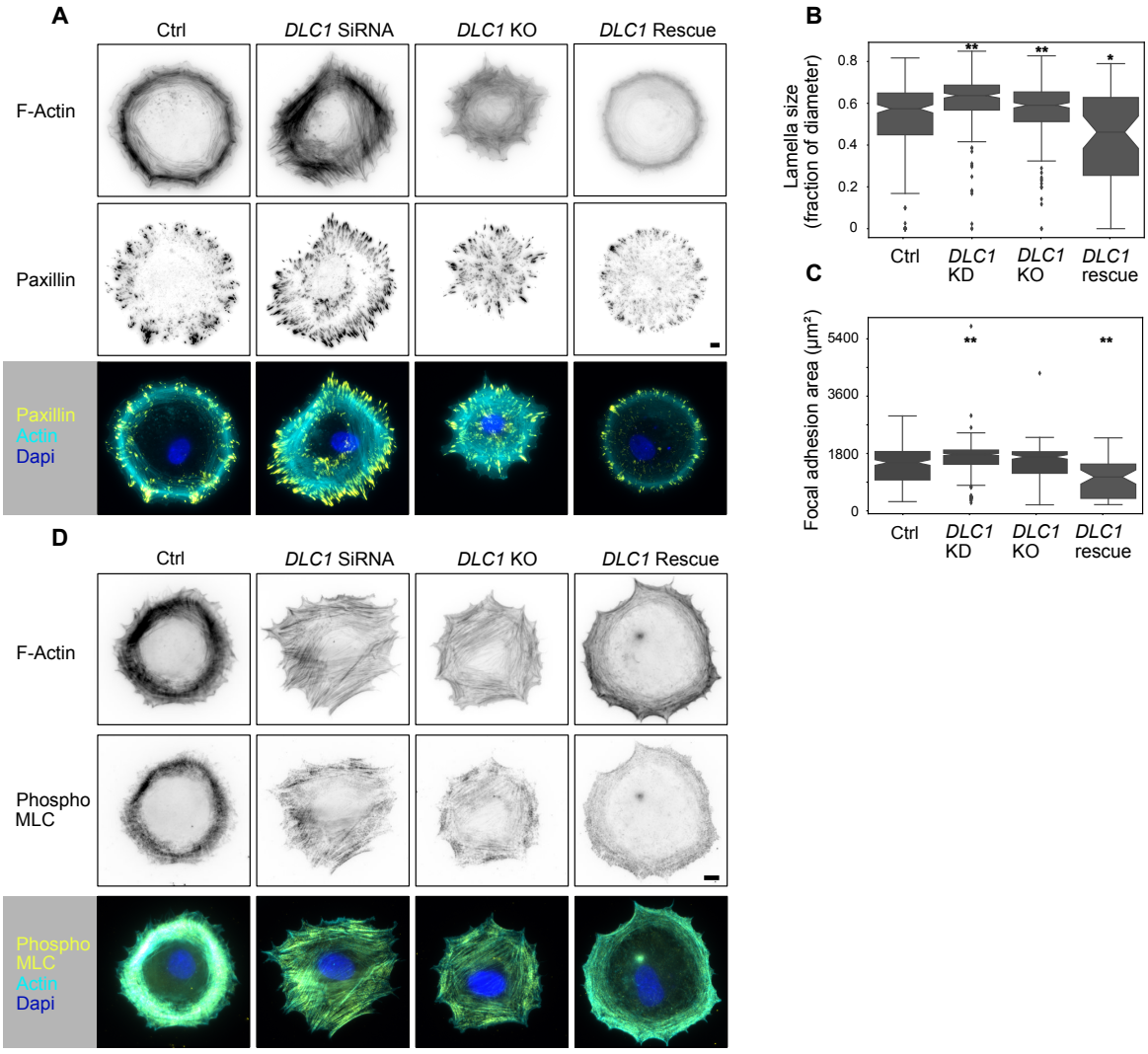

Figure 2. F-actin dynamics and cell morphodynamics in WT and *DLC1* KO cells.

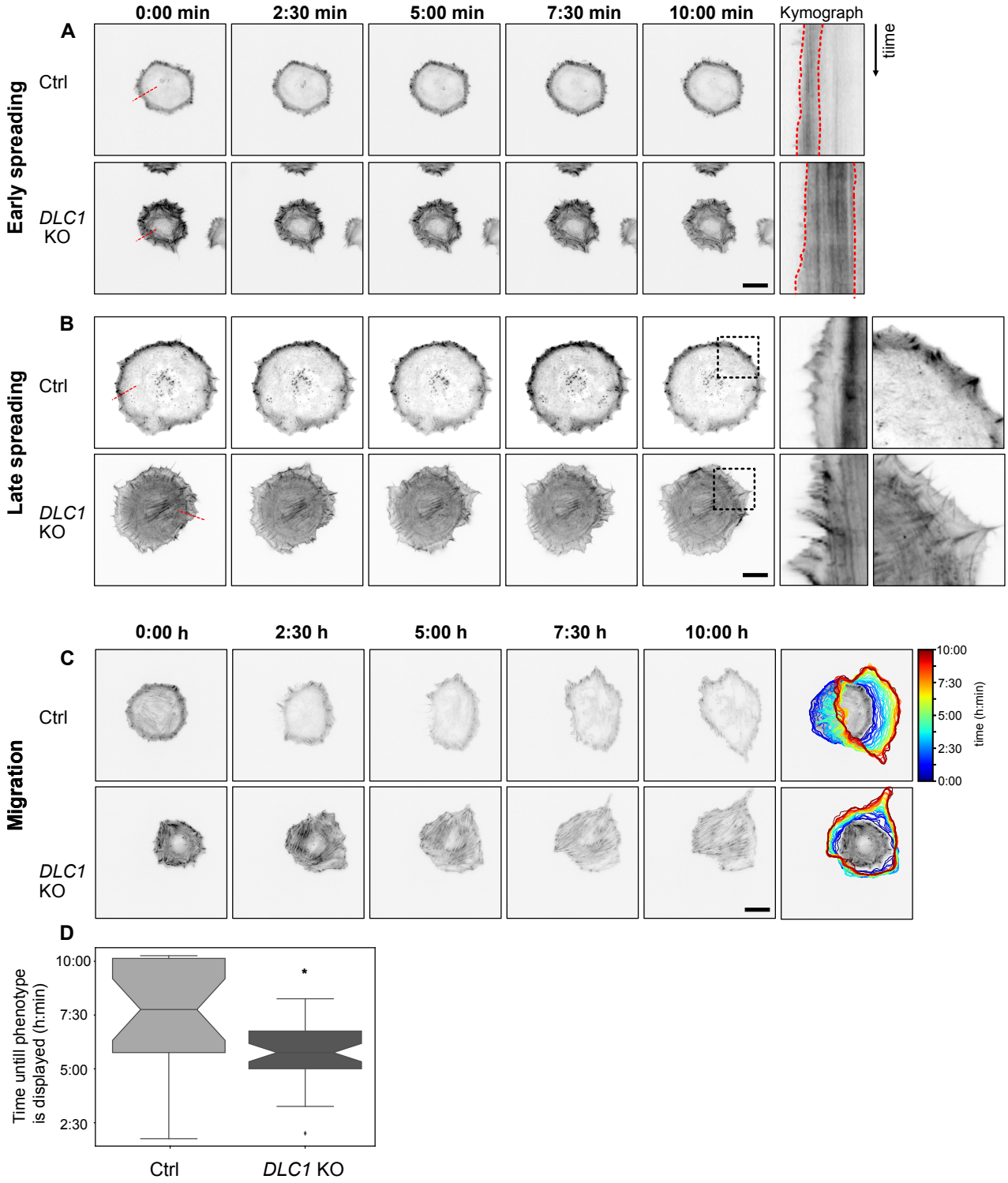

Figure 3. RhoA activation dynamics in WT and *DLC1* KO cells.

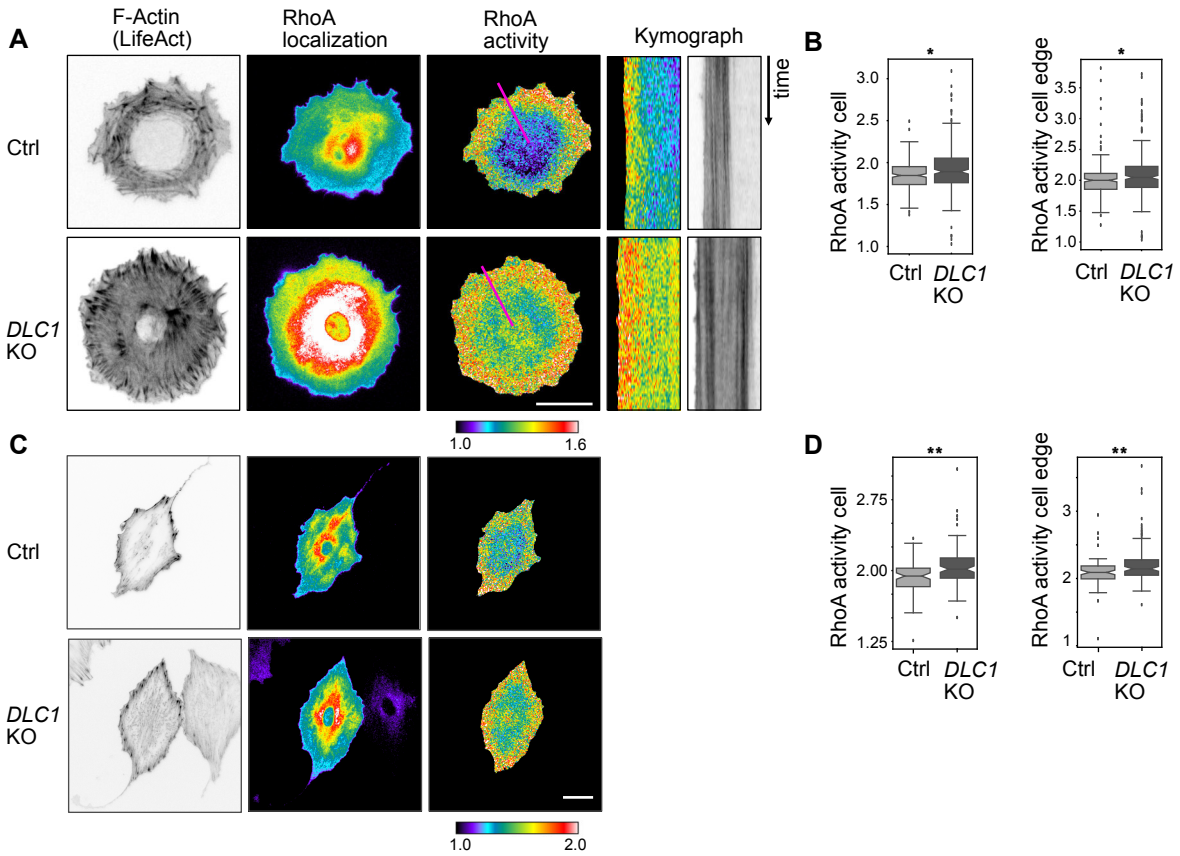

Figure 4. An optogenetic actuator- Rho biosensor circuit to probe Rho GTPase flux.

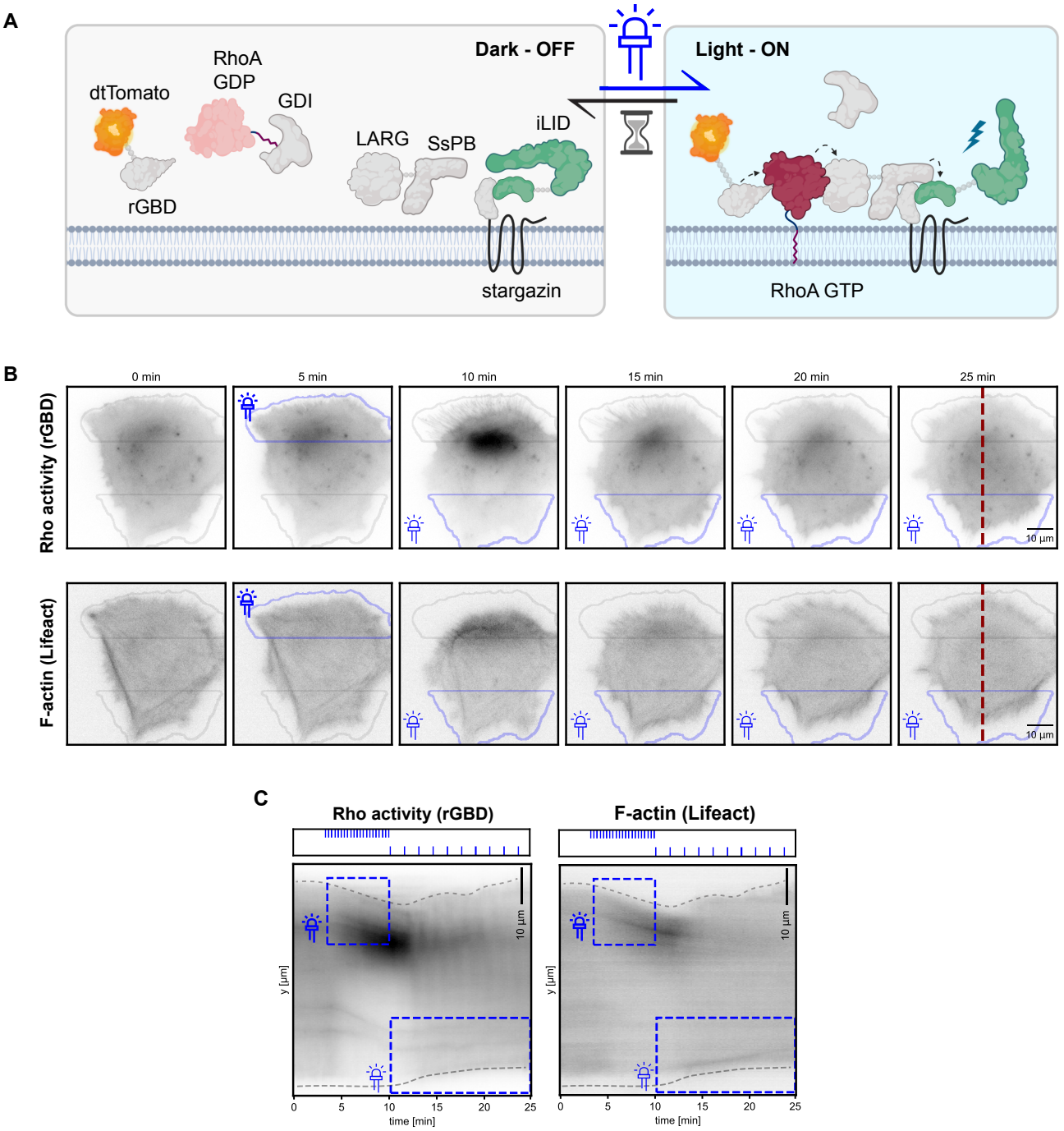

Figure 5. Rho GTPase activation kinetics in WT versus DLC1 KO cells.

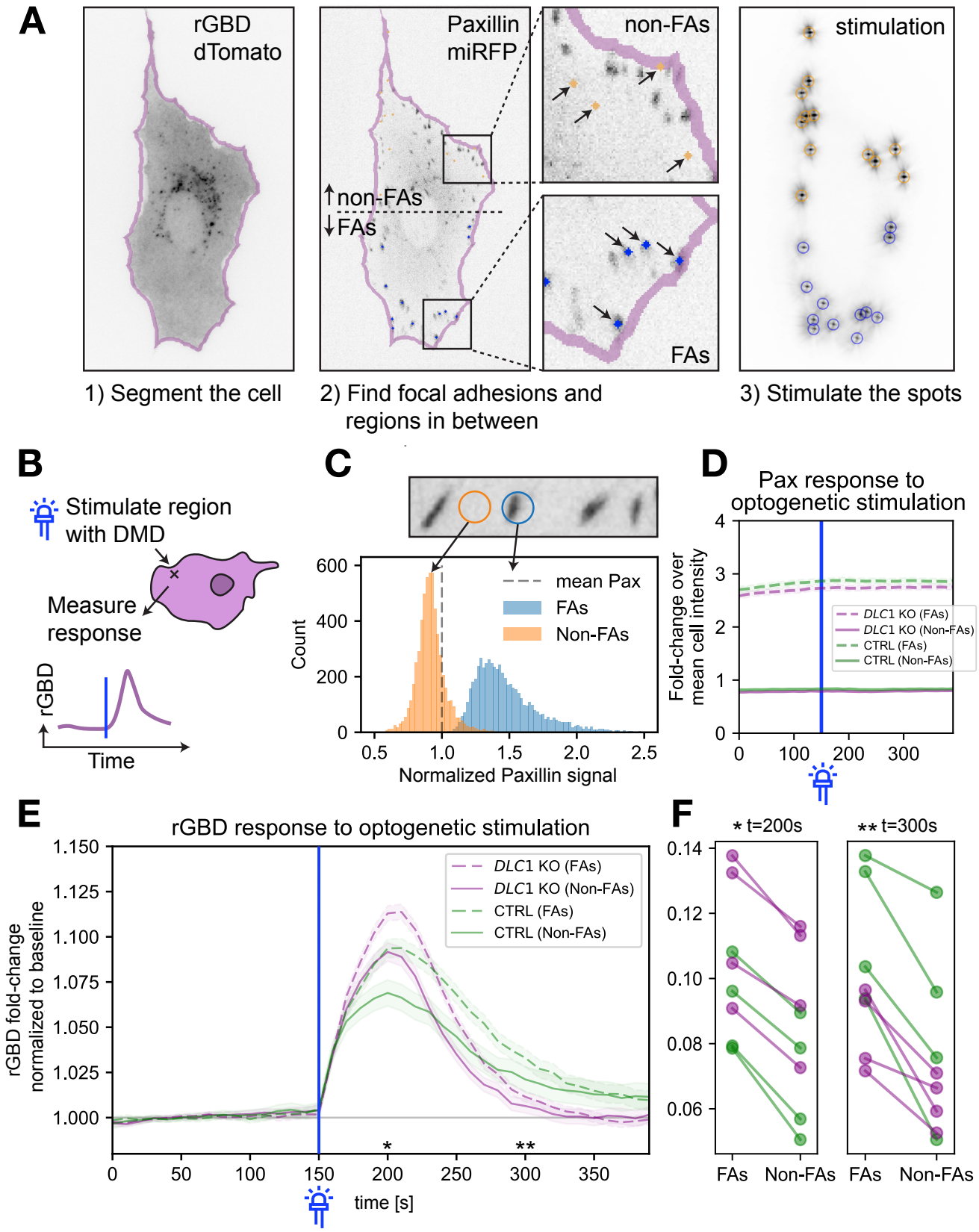

Figure 6. Mathematical Model of RhoA differential activation/deactivation dynamics in WT vs. *DLC1* KO cells.

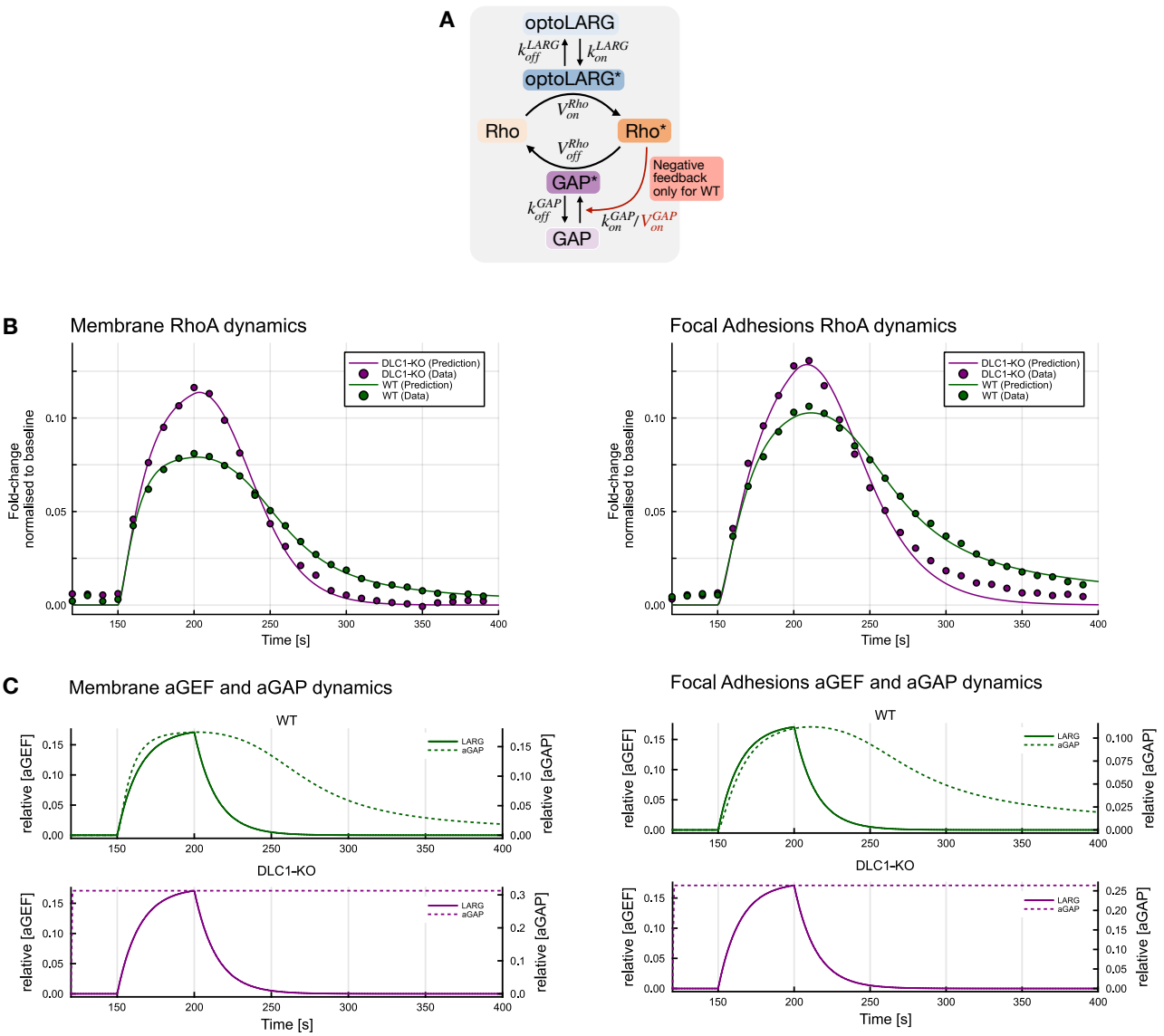

Figure 7. Optogenetic control of force-dependent DLC1 interactions with FAs.

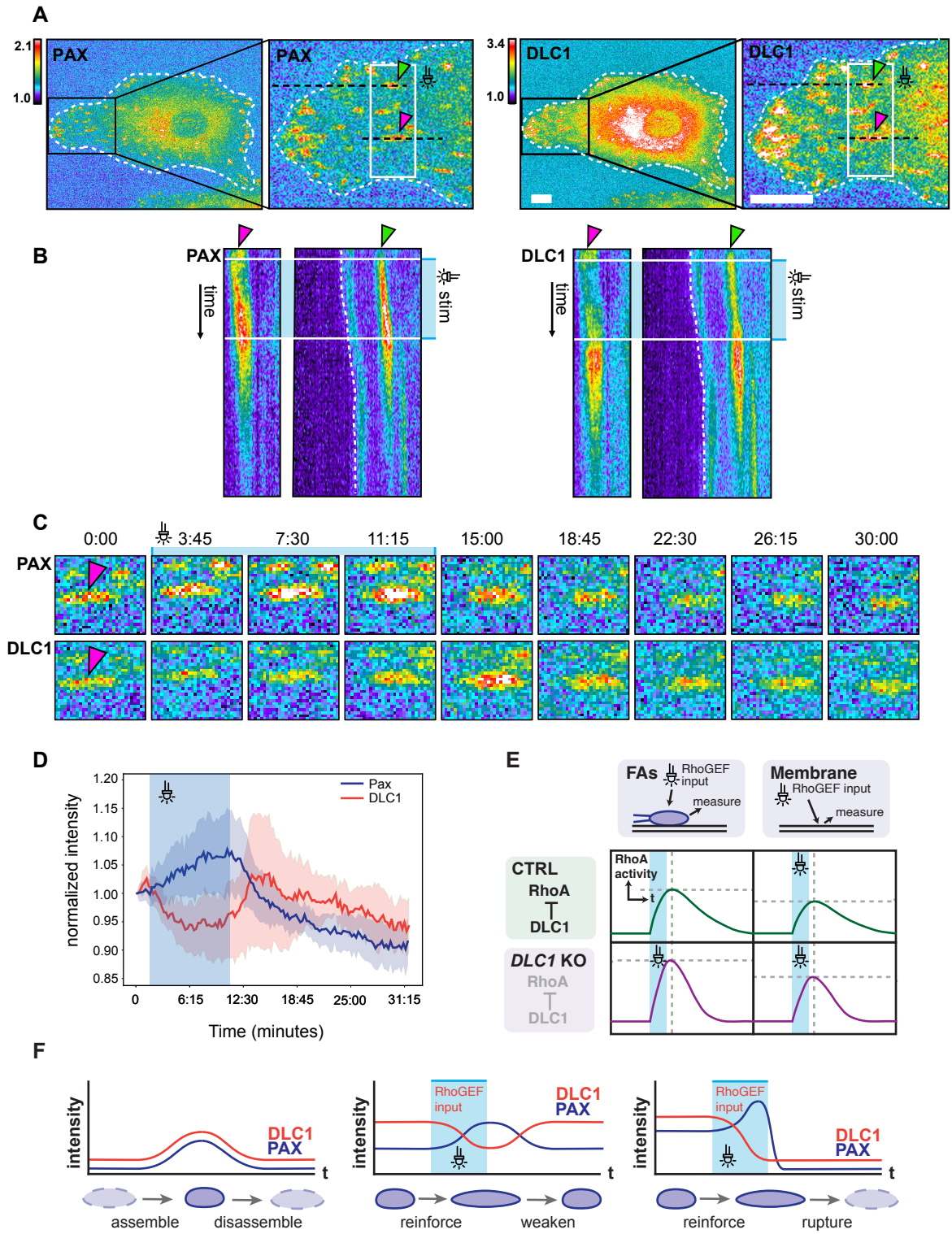

Figure S1: Cell motility properties in WT versus DLC1 KO cells.

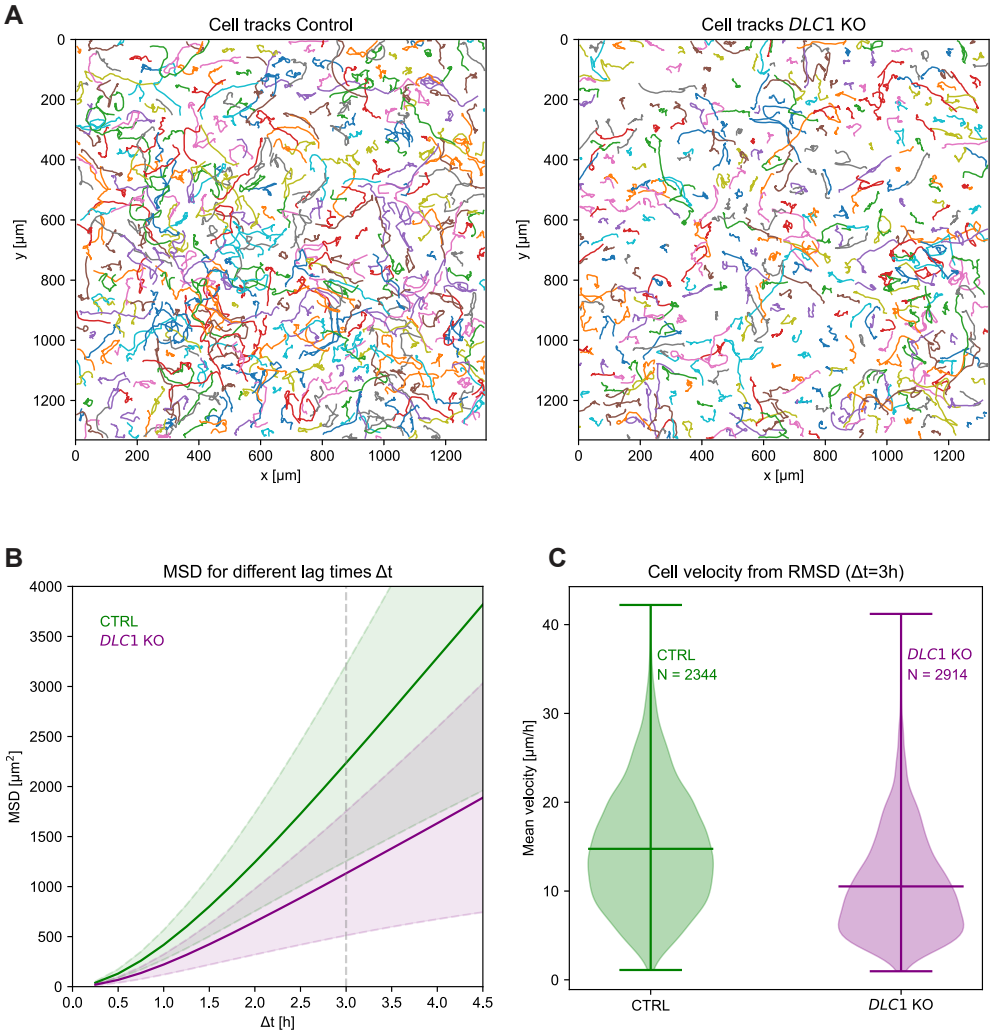

Figure S2. Effect of DLC1 overexpression on F-actin cytoskeleton and RhoA activity.

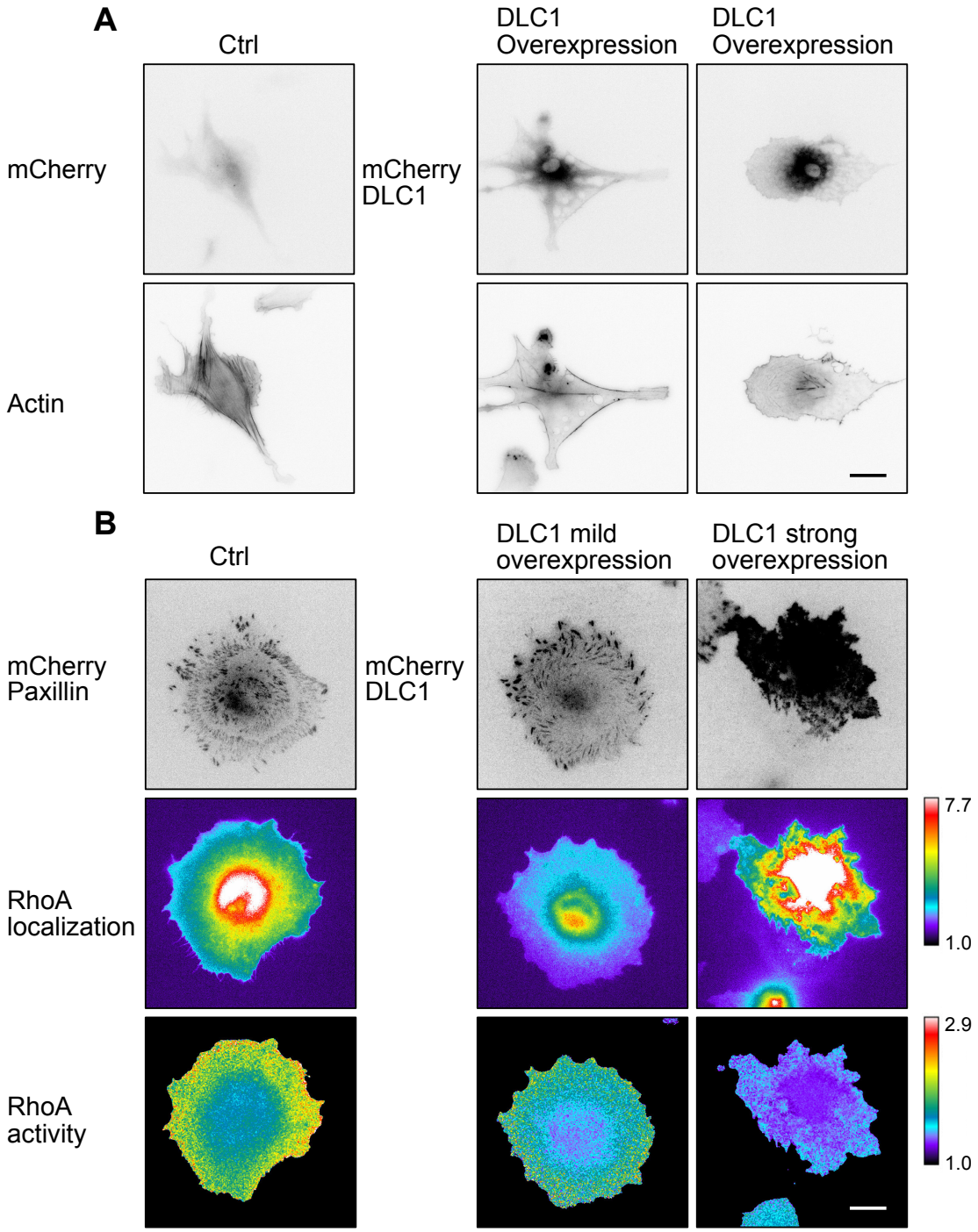

Figure S3: Quantification of optoLARG recruitment dynamics to subcellular locations.

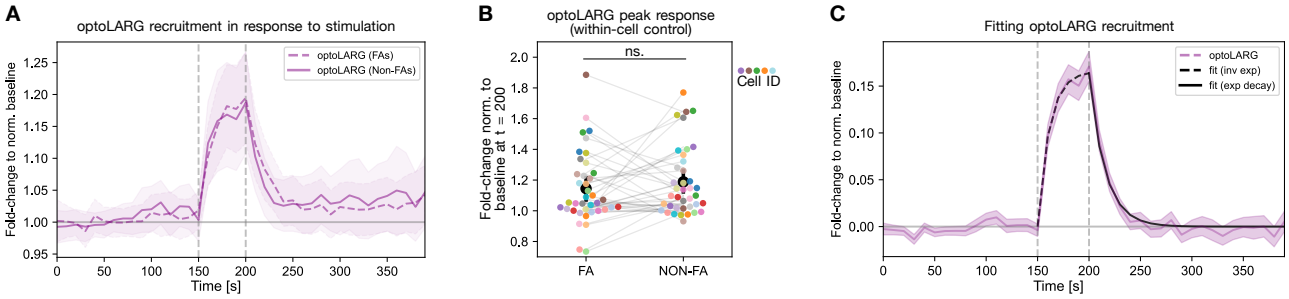

Figure S4. DLC1 dynamics at FAs in unperturbed cells.

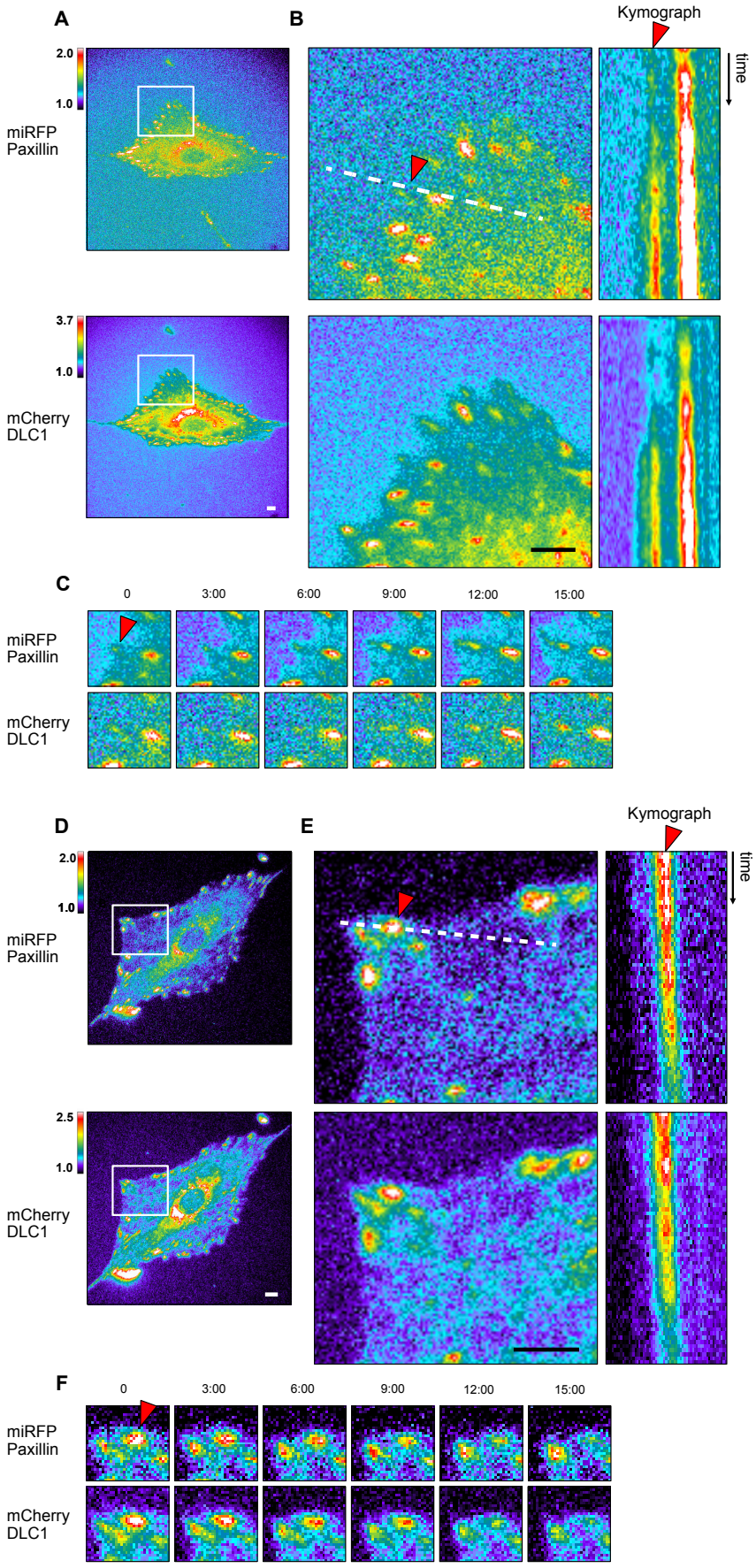
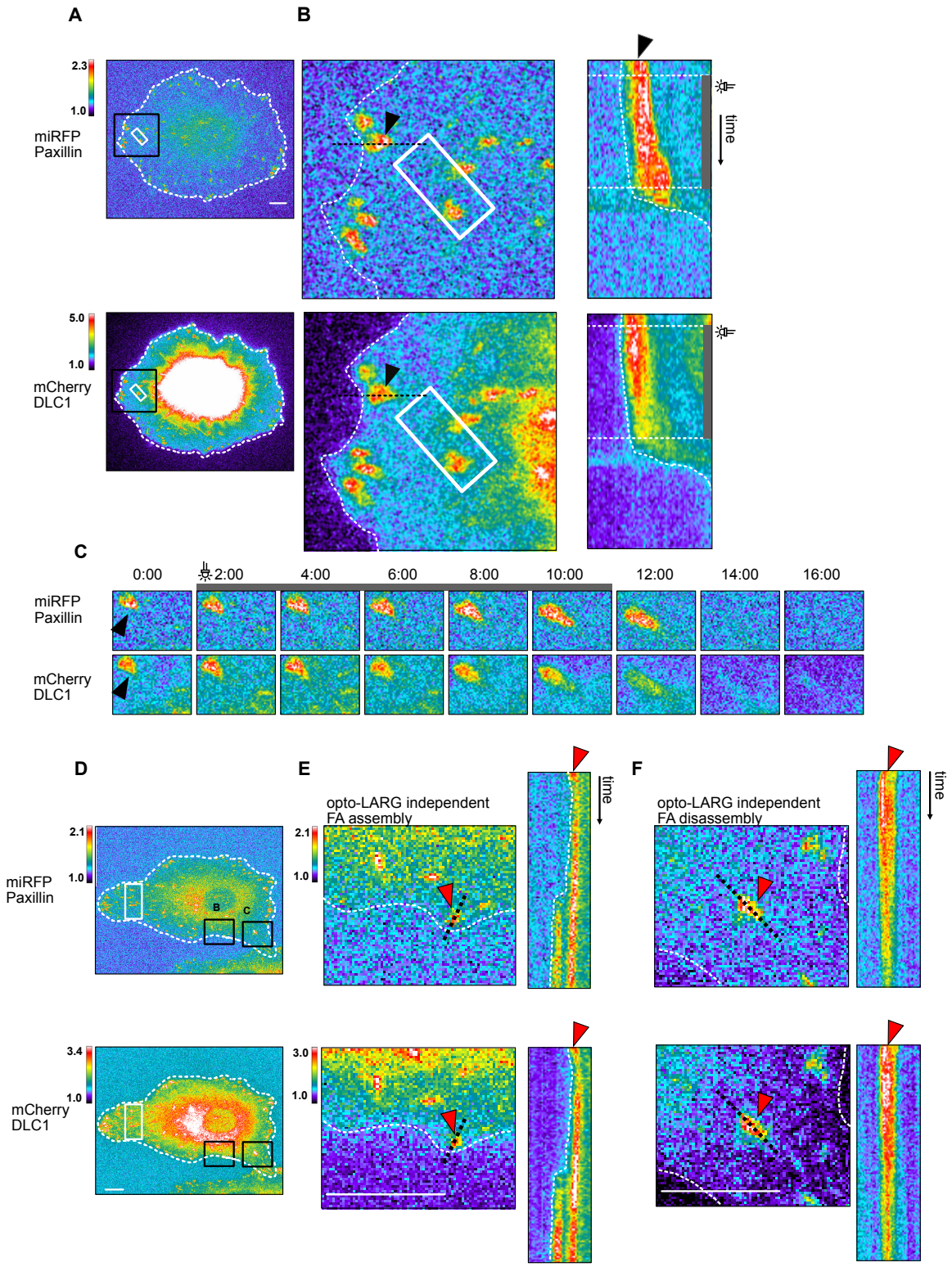
Figure S5. DLC1 dynamics in an optoLARG stimulated FA that undergoes reinforcement followed by disassembly, as well as FA behavior in absence of optoLARG stimulus.